Atmos. Chem. Phys., 25, 13493–13525, 2025 https://doi.org/10.5194/acp-25-13493-2025 © Author(s) 2025. This work is distributed under the Creative Commons Attribution 4.0 License.





Measurement report: Microphysical and optical characteristics of radiation fog – a study using in situ, remote sensing, and balloon techniques

Katarzyna Nurowska¹, Przemysław Makuch², and Krzysztof Mirosław Markowicz¹

¹Faculty of Physics, Institute of Geophysics, University of Warsaw, Pasteura 5, 02-093 Warszawa, Poland ²Institute of Oceanology, Polish Academy of Sciences, Powstańców Warszawy 55, 81-712 Sopot, Poland

Correspondence: Katarzyna Nurowska (katarzyna.nurowska@fuw.edu.pl)

Received: 20 December 2024 – Discussion started: 17 February 2025 Revised: 25 July 2025 – Accepted: 1 August 2025 – Published: 23 October 2025

Abstract. Based on in situ observations, remote sensing, and tethered balloon soundings, this study examines vertical profiles of microphysical and thermodynamic properties in radiative fog layers in the Strzyżów valley (Southeastern Poland). During three radiation fog events in September 2023, 74 soundings were performed, with 41 employing the OPC-N3 instrument to capture droplet spectra. All cases showed similar conditions, with liquid water path consistently above $15 \, \mathrm{g \, m^{-2}}$, placing most observations within the thin fog regime. Effective droplet radius decreased with height (3–4.6 μ m over 100 m), while larger droplets (18.5 μ m) were near the ground.

Fog dissipation occurred from both top and bottom. The mature stage showed peaks in liquid water content (LWC) and droplet number concentration (N_c) at about 80% of fog depth. Larger droplets (\geq 18.5 µm) were removed within minutes, affecting fog longevity. Equivalent adiabaticity (α_{eq}) – the scaling of adiabatic lapse rate to match observed liquid water path (LWP) – ranged from 0 to 0.6, with one rare case of negative nearground α_{eq} . Instruments above and below the fog allowed estimation of effect of the fog's impact on radiation flux. The difference of total shortwave and longwave NET (downward – upward) radiation at ground level before and after dissipation reached 150 W m⁻². A linear relationship was found between reduction in longwave radiation and LWP under optically thin conditions. Mean LWC in the fog core ranged from 0.2–0.4 g m⁻³, and N_c reached 300 cm⁻³. Near-surface effective radius was 8–10 µm, decreasing with height. Agreement between model outputs and observed fluxes supports the retrieved microphysical parameters.

1 Introduction

A characteristic feature of radiation fogs is their localized nature, as they do not cover large areas, making their fore-casting challenging. Weather conditions contribute to approximately 30% of aviation accidents in the USA (Gultepe, 2023). Radiation fog significantly reduces visibility and complicates navigation, posing a threat to transportation. According to the American National Transportation Safety Board (NTSB), fog is the second-most-critical weather-related factor leading to fatal aviation accidents, accounting for an estimated 14% of such incidents (Capobianco and Lee, 2001). Fog not only affects safety but also imposes significant economic costs. It can disrupt road traffic, force ships

to alter their routes, and result in airport closures. In the USA, weather is the leading cause of aircraft delays, accounting for over 70% of all cases (Kasper, 2016). Among weather-related factors, low visibility and low cloud ceilings are major contributors, as they require increased spacing between landing aircraft to maintain safety, thereby reducing airport throughput. According to NTSB data, visibility-related conditions contribute to approximately 30%–35% of all flight cancelations (Stevens, 2019; Gultepe, 2023).

Fog is a meteorological phenomenon occurring near the Earth's surface, characterized by the suspension of water droplets in the air, significantly reducing visibility to below 1 km (George, 1951). Several types of fog exist, depending on their formation mechanisms. This article focuses on ra-

diation fog, which primarily forms at night under clear-sky and minimal wind conditions, within a stable boundary layer (SBL). Under such conditions, the ground surface cools significantly, leading to the cooling of the air immediately above it (Lakra and Avishek, 2022). Once the dew point temperature is reached, water vapor condenses on suspended particles (condensation nuclei), forming fog. This type of fog develops from the ground upwards, usually not exceeding 200 m in height. The cooling of successive air layers occurs from the lower layer upward, which is why radiation fogs are associated with the formation of temperature inversions. After sunrise, and with the onset of stronger winds, the fog and the inversion dissipate. When radiation fog forms, it initially remains optically thin to longwave (LW) radiation and develops within a stable lapse rate. When fog becomes optically thick, cooling occurs predominantly at the top of the fog layer, while the portion near the ground radiates in the LW range that is able to warm the surface (Mason, 1982; Price, 2011). The potential equivalent temperature becomes uniform throughout the fog layer, inducing slight instability, which in turn increases turbulence within the fog. As demonstrated by Price (2011), approximately 50 % of the fog cases he analyzed transitioned into optically thick, well-mixed fogs characterized by a saturated adiabatic stability profile. His research suggests that this conversion typically occurs when the fog layer exceeds 100 m in thickness. Numerical weather models have difficulty catching the shift from optically thin to optically thick fog (Poku et al., 2021; Boutle et al., 2022; Antoine et al., 2023).

Costabloz et al. (2025) studied fog development during the SOFOG3D experiment. They proposed several methods to identify the point at which the transition from thin to optically thick fog occurs:

- Surface LW net radiation should approach 0. In their research they assumed that this condition occurs when $|LW_N| < 5 \, \text{W m}^{-2}$.
- The air temperature profile within the fog layer should decrease with height, as the air near the surface is warmed by the ground while the fog top cools radiatively. They checked whether the temperature gradient was negative by comparing temperatures at 25 and 50 m
- Turbulent kinetic energy exceeds $0.10 \,\mathrm{m}^2\,\mathrm{s}^{-2}$.
- Fog top height exceeds 110 m.
- Wærsted et al. (2017) proposed that a transition to optically thick fog occurs when LWP $> 30 \,\mathrm{g}\,\mathrm{m}^{-2}$, but Costabloz et al. (2025) suggested a value of $15 \,\mathrm{g}\,\mathrm{m}^{-2}$ to match the time when the other criteria are met more closely.

These conditions were met in the SOFOG3D experiment within about 1 h.

Key factors influencing the likelihood of fog transitioning into an optically thick state include the time of its formation (the earlier before sunrise, the more likely) and the humidity profile of the air (Boutle et al., 2018). For droplets to begin forming, aerosols acting as cloud condensation nuclei (CCN), such as ammonium nitrate aerosols, are required. In clouds, turbulence can uplift air masses, activating CCN more rapidly and extensively. In fog, droplet growth is primarily governed by radiative cooling. As demonstrated by Boutle et al. (2018), a higher concentration of large aerosol particles accelerates the transition to a well-mixed fog state. Additionally, the type of aerosol present in the air is important; compounds with high hygroscopicity that can activate at low supersaturation levels are most effective as CCN (Gilardoni et al., 2014).

According to Costabloz et al. (2025), during the SO-FOG3D, inverted LWC profiles – maximum LWC found at the ground and decreasing with altitude – were commonplace in optically thin fogs. Mostly in well-mixed optically thick fogs, quasi-adiabatic profiles with LWC increasing with height were found. However, in one case, they measured LWC profiles decreasing with height 1 h after the transition occurred and LWC values at the ground reached 0.25 g m $^{-3}$, the highest values recorded during the whole campaign.

Research utilizing cloud radars, ceilometers, and microwave radiometers has made it possible to establish the rate at which LW radiative cooling at the top of the fog layer can lead to condensation within the fog. Under clear-sky conditions, when the liquid water path (LWP) exceeds $30\,\mathrm{g\,m^{-2}}$, this cooling (above the fog) can result in the formation of liquid water at a rate of up to $70\,\mathrm{g\,m^{-2}\,h^{-1}}$ (Wærsted et al., 2017).

The presence of clouds above the fog can also influence water condensation, with low clouds potentially blocking cooling entirely, leading to fog dissipation.

After sunrise, shortwave (SW) radiation begins to heat the fog, causing droplet evaporation. Wærsted et al. (2017) estimated that the strength of this process is about $10-15\,\mathrm{g\,m^{-2}\,h^{-1}}$. The rate of evaporation increases with the effective radius of droplets (r_{eff}) and LWP and decreases with larger solar zenith angles. Additionally, the warming of the ground surface transfers approximately $30\,\mathrm{g\,m^{-2}\,h^{-1}}$ of sensible heat to the fog.

To accurately predict the formation and evolution of fog, a weather forecasting model must effectively represent the interactions between the atmosphere and the Earth's surface, including various processes (such as microphysics, radiation, and turbulence), and it must do so on a local scale while accounting for terrain features.

One approach to studying fog is through large eddy simulation (LES) modeling. This approach enables the examination of turbulence effects and interactions between the atmosphere and the surface (Maronga and Bosveld, 2017), the deposition of droplets on vegetation (Mazoyer et al., 2017), or the influence of the urban canopy (Bergot et al., 2015) on fog

formation and evolution. Numerical models often struggle to accurately forecast fog formation, dissipation, depth, or water content (Román-Cascón et al., 2012; Zhou et al., 2012; Bari et al., 2023). This difficulty arises from the fog's localized nature and the delicate balance between processes such as radiation balance, droplet deposition on the surface, turbulent mixing, microphysical properties, and moisture availability. Recently, AI-based tools, including machine learning and deep learning, have been employed to enhance numerical weather prediction (NWP). While these methods have shown promising results, they also introduce new challenges. Machine learning requires high-quality datasets specific to each forecast location, as well as substantial computational resources to produce timely results (Bari et al., 2023).

For the initialization of numerical models or the development of methods to retrieve LWP from satellites, it is essential to understand the microphysical properties of fog as a function of height. Unfortunately, there is a scarcity of data on the vertical distribution of fog's microphysical characteristics. Measurements using aircraft are impractical because fog typically forms close to the Earth's surface and inherently reduces visibility. However, measurements can be conducted using aerological balloons (Egli et al., 2015) and instrumentation placed on tall towers (Ye et al., 2015; Han et al., 2018), and more recently, drones and microwave radiometers (MWRs) have become viable options for such observations.

Using a tethered balloon, Pinnick et al. (1978) made the first measurements of the vertical profiles of microphysical characteristics in fog. They showed that in the studied cases, fog had a bimodal distribution of droplets (r = 5 and $r = 0.6 \,\mu\text{m}$) with a LWC range from 10^{-4} to $0.45 \, \text{g m}^{-3}$.

Egli et al. (2015) performed soundings with a tethered balloon and measured LWC, N_c , and $r_{\rm eff}$ every 10 m. His results from two fog cases show that the changes in LWC are related to the change in N_c and not to the change in droplet size. In most cases, r_{eff} was constant with height. One fog case was characterized by low LWC (maximum of 0.14 g m⁻³) but high $N_{\rm c}$ above 2000 cm⁻³. In this case of fog, three measurements were taken. Omitting the values of $r_{\rm eff}$ at the very bottom of the profiles (where the values dropped significantly), the value of $r_{\rm eff}$ decreased with height. In the case of one profile, the value of $_{eff}$ at a 25 m reached a maximum of 9.4 μm . The second fog case, with six soundings, consisted of considerably thicker fog with higher LWC and $r_{\rm eff}$ values, although it was accompanied by lower total drop counts. The LWC had a constant pattern in the first third of the height, then it increased with height, and then it decreased with height to the cloud top. The highest LWC value was $0.54 \,\mathrm{g \, m^{-3}}$. $N_{\rm c}$ had a similar pattern with height to LWC. The highest N_c value recorded was $500 \,\mathrm{cm}^{-3}$. The r_{eff} values differ from sounding to sounding; however they were constant with height, in the range between 4 and 8 µm.

The motivation for this study is the miniaturization of equipment for particle detection. For example, the Al-

phasense OPC-N3, an optical particle matter (PM) sensor commonly used for aerosol monitoring, can also be used to measure the microphysical properties of fog when mounted on a tethered balloon or drone (Nurowska et al., 2023). Such a system was employed to capture vertical profiles of radiative fog in a mountain valley, a region where air pollution can be elevated during inversion conditions. This type of terrain enables fog monitoring at different altitudes. In this setup, SW and LW radiometers positioned near the valley bottom and mountain top allow determination of the optical, microphysical, and radiation closure of the fog. Section 2 outlines the instruments utilized for conducting the measurements, while Sect. 3 details the methodology of the in situ measurements and the model setup. The core of the article is presented in Sect. 4, which features a case study of radiative fog occurrence, including optical, microphysical, and radiation closure analyses performed for this case. Section 4 focuses on an event in the Strzyżów valley, where data were gathered using a balloon. The 1D Fu-Liou radiative transfer model (Fu and Liou, 1992, 1993) was applied to simulate the conditions in the Strzyżów valley, incorporating additional data from the SolarAOT station (which consists of an upper and lower station).

2 Experiment setup

This study is based on measurements taken at two sites in Strzyżów. This small town is located in southern Poland, in the region of the Strzyżowskie foothills. The city is located next to the Wisłok River. The research was conducted using remote sensing and in situ techniques as well as an apparatus connected to a tethered balloon. In addition, numerical simulations were used for the radiation closure study.

2.1 SolarAOT_{lower} launching site

The lower station is located in the valley of the city of Strzyżów at 260 m a.s.l. (49°52′18.0″ N, 21°48′26.0″ E). A CNR4 net radiometer was mounted on the site of balloon launching, for upward and downward SW and LW flux, as well as a meteo station including MetPak and sensors A100LK, W200P, HYT936, and OPC-N3. In addition, the mobile laboratory equipped with Aurora 4000 nephelometer, Laser Aerosol Spectrometer LAS 3340A, and Oxford Lasers VisiSize D30 (ShadowGraph) was used at this site. Raymetrics single-wavelength (532 nm) lidar 510M for aerosol and cloud detection was used.

The VisiSize D30 system, developed by Oxford Lasers Ltd., operates using the shadowgraph technique. The VisiSize D30, hereafter referred to as ShadowGraph, captures shadow images of particles as they pass through the measurement volume between a laser head and a high-resolution camera. This system enables the determination of microphysical properties, including particle shape, size, droplet size

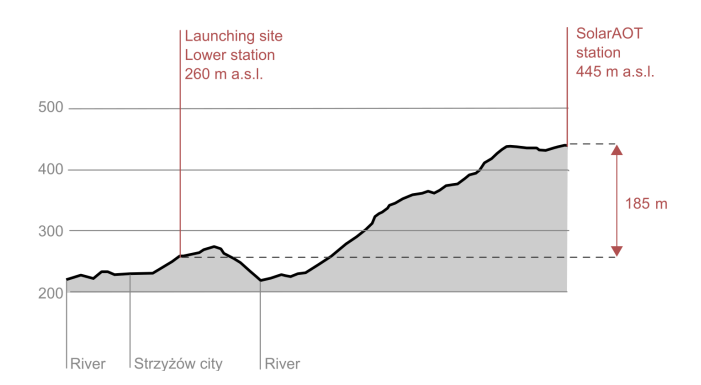


Figure 1. Location of tethered balloon launching site SolarAOT_{lower} and SolarAOT^{upper} station, in relation to the city of Strzyżów and the Wisłok River.

distribution (DSD(r)), total droplet number concentration, and liquid water content (LWC).

The ShadowGraph system has been effectively utilized in the study of cloud microphysics, both in laboratory settings and during in situ measurements. The droplet detection and sizing mechanisms of the ShadowGraph were comprehensively detailed by Nowak et al. (2021). Data collected using the ShadowGraph in studies of orographic clouds, specifically under foggy conditions in mountainous regions, were analyzed by Mohammadi et al. (2022).

During this campaign, the ShadowGraph was used for two purposes: first, as the reference instrument to which the OPC-N3 was calibrated, as demonstrated in Nurowska et al. (2023), and second, to monitor conditions near the surface. The ShadowGraph operates using a high-power laser with a wavelength invisible to the human eye. For safety reasons, it was installed on the roof of the mobile laboratory, approximately 3 m above ground level.

2.2 SolarAOTupper station

SolarAOT^{upper} is a private radiative transfer research station (which collaborates with the University of Warsaw) located in an agricultural area on one of the peaks of the Niebylecka Mountain at 445 m a.s.l. (49°52′43.0″ N, 21°51′40.8″ E), located away from the city of Strzyżów in a straight line of 4 km with a vertical height difference 185 m. The location of both stations is shown in Fig. 1. Several instruments are mounted at the SolarAOT^{upper} station, inter alia, pyranometer CMP21, Eppley pyrgeometer, CIMEL, Nephelometer Aurora 4000, Aethalometr AE-31, and CHM-15K ceilometer.

A Kipp & Zonen CMP21 pyranometer was used to measure downwelling shortwave radiation (285–2800 nm), including both direct solar and diffuse sky components. For longwave radiation, an Eppley pyrgeometer was employed, operating in the spectral range of approximately 4.5 to 50 μ m, to capture downwelling infrared radiation emitted by the at-

mosphere and clouds. Both sensors were installed on a leveled platform in an unobstructed area.

CIMEL is an instrument for measuring direct and scattered solar radiation in nine spectral channels: 340, 380, 440, 500, 675, 870, 936, 1020, and 1640 nm. Based on the measured values, the optical parameters of the aerosol are determined, including the AOD and the Ångström exponent. The data collected by the instrument is processed within the international AERONET measurement network. Nephelometer Aurora 4000 is used to measure light scattering coefficients on aerosols for wavelengths of 450, 525, and 630 nm in 18 ranges of aerosol scattering angles.

Aethalometer AE-31 is used to measure the concentration of equivalent black carbon (eBC) in the atmosphere and the aerosol absorption coefficient of the aerosol. The measurement is performed at seven wavelengths (370, 470, 520, 590, 660, 880, and 950 nm) using the method of changing the transmission of a quartz filter on which the aerosol is deposited.

2.3 Balloon apparatus

Measurements were conducted using two meteorological balloons (for better buoyancy), each approximately 1.5 m in diameter and filled with helium. The balloons were tethered using the Vaisala TTW111 winch (see Fig. 2a). Around 2 m below the balloon, the apparatus was mounted on the rope holding the balloon. The apparatus used to mount below the balloon was as follows (see Fig. 2b):

- Vaisala radiosonde RS41 collecting data about pressure (p), temperature (T), and relative humidity (RH);
- GY-63 MS5611 a high-performance pressure sensor module;
- HYT 939 additional T and RH sensor;
- the Alphasense OPC-N3 an optical particle sensor that measures particle counts across size bins ranging from 0.35 to 40 μm, as well as $PM_{1.0}^{-1}$, $PM_{2.5}$, and PM_{10} here, OPC-N3 was used to gather information about fog droplets based on the article (Nurowska et al., 2023), such as liquid water content (LWC), effective radius $r_{\rm eff}$, and $N_{\rm c}$ –
- SENSIRION SPS30 an optical PM sensor that measures PM_{1.0}, PM_{2.5} PM₄, and PM₁₀ mass concentration;
- TFMini a visibility sensor;
- AE-51 a miniature aethalometer for measuring the eBC concentration and the aerosol absorption coefficient at a wavelength of 880 nm.

¹The number after PM denotes particles that are counted with diameters up to the given size in μm.

The OPC-N3, an optical particle counter designed by Alphasense Ltd., utilizes a diode laser emitting light at a wavelength of 658 nm, along with an elliptical mirror that directs the laser beam towards a detector. The airflow, driven perpendicularly to the laser beam by an integrated fan, allows for continuous operation. The OPC-N3 quantifies particle number concentration (N_c) across 24 size bins, covering a diameter range from 0.35 to 40 µm. The onboard algorithm converts N_c measurements into PM₁, PM_{2.5}, and PM₁₀ values. Detailed specification of the OPC-N3 is available in the work by Hagan and Kroll (2020).

OPC-N3 devices are considered low-cost sensors, which means that two identical units may not yield consistent results due to device-to-device variability. Therefore, cross-calibration between sensors or calibration against a reference-grade instrument is necessary to ensure measurement accuracy. Additionally, individual OPC-N3 units may exhibit signal drift over time, requiring periodic recalibration to maintain data reliability.

For this reason, it was not possible to directly use the calibration parameters provided in Nurowska et al. (2023). Instead, the calibration had to be repeated following the methodology described in that work, to ensure compatibility with the specific sensors used in this study. OPC-N3 was calibrated to the ShadowGraph following Nurowska et al. (2023). Results of N_c , LWC, and $r_{\rm eff}$ were obtained by taking bins of OPC-N3 measuring particles greater than 1.15 μ m (bin 7 of OPC-N3).

The calibration equations used between OPC-N3 and Shadowgraph are as follows:

$$LWC_{ShadowGraph} = 6.15 \cdot LWC_{OPC-N3} + 0.11 \tag{1}$$

$$N_{\text{cShadowGraph}} = 4.16 \cdot N_{\text{cOPC-N3}} + 32.63 \tag{2}$$

$$r_{\text{eff}}^{\text{ShadowGraph}} = 0.70 \cdot r_{\text{eff}}^{\text{OPC-N3}} + 3.81. \tag{3}$$

The OPC-N3 allows calculation of the volume droplet size distribution (vDSD), which can be computed using the following formula:

$$vDSD(r_b) = N_b \cdot (\Delta r_b \cdot V_b)^{-1} \cdot r_b^3, \tag{4}$$

where N_b is the number of droplets in a bin, V_b is the volume of a bin, Δr_b is the width of the bin, and r_b is the mean bin droplet radius. Although the obtained vDSD was not calibrated against the ShadowGraph, it provides information on which droplet sizes contribute most significantly to the LWC at a given altitude.

3 Methodology and model setup

3.1 Balloon measurement methodology

For 3 d between 9–11 September 2023, the measurements of radiative fog were made in the city of Strzyżów, Poland. The balloon launch site was located in the valley of the city of

Strzyżów. Four setups were used, as it was not possible to mount all instruments at once due to the buoyancy:

- setup 1: GY-63, HYT 939, OPC-N3, SPS30, TTFMini
 this setup was most common;
- setup 2: only Vaisala radiosonde RS41;
- setup 3: Vaisala radiosonde RS41, AE-51;
- setup 4: Vaisala radiosonde RS41, GY-63, HYT 939, OPC-N3, SPS30, and TFMini.

With colored lines, Fig. 3 shows when, during the night, the soundings were done, with colors indicating different setups mounted on the balloon. The same information, but with specific sounding times, can be found in Appendix B2. In total, 74 soundings were conducted. However, due to data recording issues, 11 soundings lacked complete data and were excluded from further analysis. These are indicated in gray in Fig. 3 and Table B2. Soundings were done by unwinding the rope until it started to tilt to the horizon. The balloon was stopped for a few seconds, and the line was wound up. Soundings were done with around 15 min breaks in between.

The fog case description was divided into three stages: initial, developed, and decaying. The transition from the initial to the developed stage was assumed to occur when LWP > $15 \, \mathrm{g \, m^{-2}}$; the change from mature to decaying was assumed when LWP < $15 \, \mathrm{g \, m^{-2}}$. Table 1 presents information about each fog stage.

During one balloon launch, we obtained two vertical profiles, which were then averaged over height to obtain a less noisy image due to random fluctuations. All the data were interpolated every 1 m for making figures. On the plots, soundings start at 2 m above ground.

3.2 Adiabatic LWC

Equivalent adiabaticity (α_{eq}) relates theoretical adiabatic LWC profiles to observed ones. It has been used in studies aiming to estimate cloud base height or improve fog forecasting based on satellite data. For instance, Cermak and Bendix (2011) proposed a model comparing theoretical and satellite-derived LWP to infer cloud base height, while Toledo et al. (2021) applied a similar approach to model fog dissipation. In this section, we present the theoretical derivation of α_{eq} , which is defined as the scaling factor applied to the adiabatic LWC profile to match the theoretical LWP with the observed value.

To describe the change of LWC in a perfect adiabatic cloud, the following equation is used (Eq. 5) (Cermak and Bendix, 2011; Toledo et al., 2021; Costabloz et al., 2025):

$$\frac{dLWC(z)}{dz} = \Gamma_{ad}(T(z), p(z)), \tag{5}$$

where z is the height calculated from the base of the cloud. $\Gamma_{\rm ad}(T(z), p(z))$ is the negative of the change in saturation



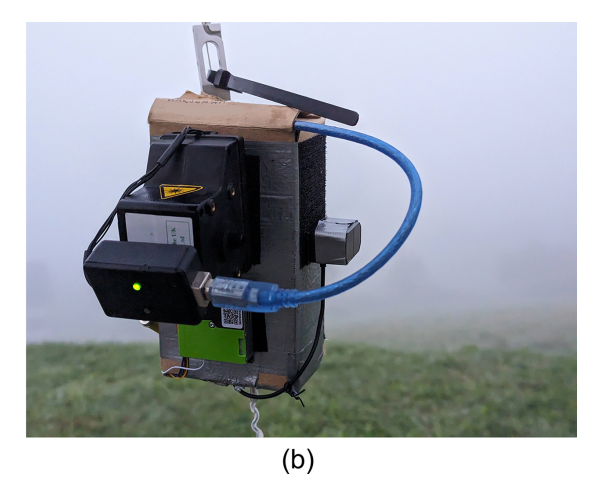


Figure 2. Balloon setup. (a) Balloon with attached payload and connected to the winch. (b) Zoomed-in view of the balloon payload, showing inside the box (GY-63, HYT 939), OPC-N3, SPS30, and TFMini.

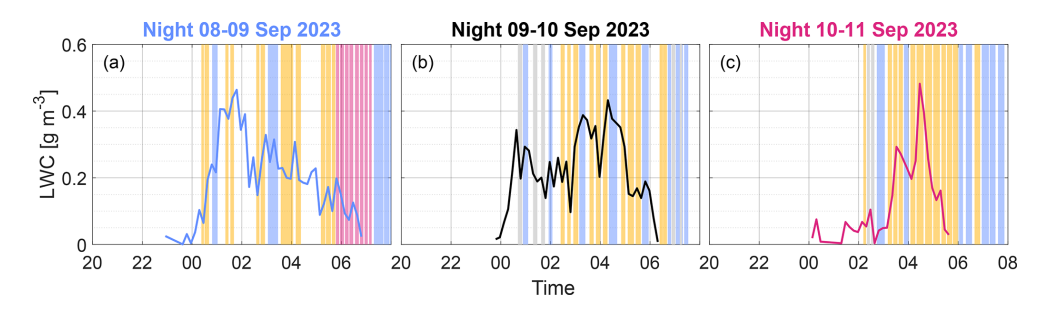


Figure 3. The figure illustrates the timing of the soundings; different colors represent the specific equipment configurations mounted on the balloon: orange - setup with OPC-N3, blue - setup with radiosonde, pink - setup with OPC-N3 and radiosonde, gray - problems with collected data. The image is overlaid on the line representing temporal variability of the LWC at the ground obtained from Shadowgraph (the same data as in Fig. 5).

mixing ratio with height for an ideal adiabatic cloud; in other words, it is the adiabatic condensation rate. The processes in stratus clouds are nearly adiabatic; the deviation from adiabatic conditions is introduced into the equation as a parameter α . The fog is similar to stratus cloud; however, to integrate Eq. (5) apart from adding α , non-zero surface liquid water content (LWC₀) must be taken into account.

$$LWC(z) = \int_{z'=0}^{z'=z} \alpha(z')\Gamma_{ad}(T(z'), p(z')) dz' + LWC_0$$

$$\approx \Gamma_{ad}(T_B, p_B) \int_{z'=0}^{z'=z} \alpha(z') dz' + LWC_0$$
stant adiabaticity value that would give the same by the many sta

LWP is defined as

$$LWP = \int_{z'=0}^{z'=CTH} LWC(z') dz'.$$
 (7)

As fog base is at the ground, the integration takes place from z' equal zero to cloud/fog top height (CTH).

In the case of shallow clouds $\Gamma_{ad}(T(z), p(z))$ can be assumed constant with height (Brenguier, 1991); $\Gamma_{\rm ad}(T_{\rm B}, p_{\rm B}) = {\rm const.}$, where $T_{\rm B}$ and $p_{\rm B}$ are temperature and pressure at fog base/ground, respectively. Since the dependence of $\alpha(z)$ is unknown, the concept of equivalent adiabaticity α_{eq} = const. is introduced. α_{eq} is defined as the constant adiabaticity value that would give the same LWP value when replacing $\alpha(z')$ in Eq. 6 and calculating LWP from Eq. (7). After taking $\alpha_{eq} = \text{const.}$ the formula for LWP be-

$$LWP = \frac{1}{2}\alpha_{eq}\Gamma_{ad}(T_{B}, p_{B}) \cdot CTH^{2} + LWC_{0} \cdot CTH.$$
 (8)

The formula for LWC with the above assumptions is

$$LWC(z) = \alpha_{eq} \Gamma_{ad}(T_B, p_B) \cdot z + LWC_0. \tag{9}$$

The method of calculating $\Gamma_{ad}(T_B, p_B)$ was taken from Appendix A of the article (Toledo et al., 2021).

Profiles with radiosonde

Stage Fog episode Initial Developed Decaying (soundings after fog vanishing) Time 23:00-02:34 02:34-06:42 06:45-07:00 (08:10) Night of 8-9 Profiles with OPC-N3 4 12 2(+1)Profiles with radiosonde 6 1 2(+4)Time 00:00-02:45 02:45-06:00 06:00-07:30 Night of 9-10 Profiles with OPC-N3 0 9 2 3 Profiles with radiosonde 1 4 Time 02:00-03:02 03:02-5:30 05:30-6:00 (08:00) Night of 10-11 Profiles with OPC-N3 7 2(+1)

1

2

Table 1. Times of initial, developed, and decaying stage of observed fogs on days 9–11 September, with information on how many soundings were performed in each period.

To calculate what α_{eq} , just reverse Eq. (8):

$$\alpha_{\text{eq}} = \frac{2(\text{LWP} - \text{LWC}_0 \cdot \text{CTH})}{\Gamma_{\text{ad}}(T_{\text{B}}, p_{\text{B}}) \cdot \text{CTH}^2}.$$
 (10)

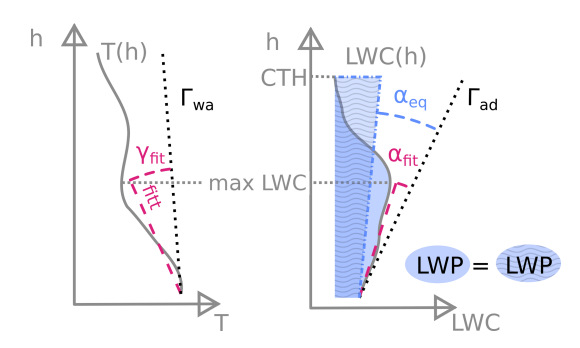
In the literature, instead of α_{eq} , the parameter β is sometimes used, introduced by Betts (1982) as the in-cloud mixing parameter. This parameter measures departure from the adiabatic situation. The relation between α_{eq} and β is $\alpha_{eq} = 1 - \beta$. In the latter part of this article, the following will be used:

- Γ_{ad} adiabatic condensation rate of LWC;
- α_{eq} scaling of Γ_{ad} , which would give the same LWP for the whole cloud/fog;
- α_{fit} scaling of Γ_{ad} obtained by fitting line to LWC dependence from height;
- Γ_{wa} moist adiabatic lapse rate for T;
- γ_{fit} scaling of Γ_{wa} obtained by fitting line to T dependence from height.

Figure 4 presents the visualization of the concepts listed above.

3.3 Radiometer data processing

At the SolarAOT^{upper} station, a CMP21 pyranometer and an Eppley pyrgeometer were installed to measure downwelling shortwave and longwave radiation, respectively. Both instruments recorded data at 42 s intervals. At the SolarAOT_{lower} station, a CNR4 net radiometer was mounted to measure both upward and downward shortwave and longwave fluxes, with a sampling interval of 36 s. Data from SolarAOT^{upper} were interpolated to match the temporal resolution of the lower



0(+5)

Figure 4. Representation of profile of T and LWC with added lines of $\Gamma_{\rm Wa}$ and $\Gamma_{\rm ad}$ respectively. $\gamma_{\rm fit}$ and $\alpha_{\rm fit}$ represents the angle between the best line fit to T and LWC, respectively (from bottom to height of max LWC), and $\Gamma_{\rm Wa}$ and $\Gamma_{\rm ad}$. $\alpha_{\rm eq} = {\rm const.}$ is defined as deviation from $\Gamma_{\rm ad}$, which would give the same LWP as the original data.

station. Short spikes in the radiometric signal – likely due to transient obstructions such as birds – were removed using a filtering algorithm. Additionally, the signal was smoothed using a 10 min running mean. The 10 min averaging window was chosen to correspond to the typical duration of balloon flights (10–15 min), allowing for comparison between the measured and simulated radiative fluxes.

3.4 1D simulation radiation fluxes

This section presents the model used to perform optical, microphysical, and radiative closure, as discussed in Sect. 4.4. The model was used to assess the consistency between observed radiation and retrieved fog microphysical properties. For this purpose, simulations were done in 1D using the Fu–Liou code (Fu and Liou, 1992, 1993).

The Fu-Liou radiative transfer model is a sophisticated tool designed to accurately simulate radiative transfer in the Earth's atmosphere. The Fu–Liou code uses δ -four-stream and δ -two-stream flux approximation, which allows it to efficiently handle the complexities of radiation scattering and absorption by gases, aerosols, and cloud particles. The model covers 6 shortwave (SW, $\lambda < 4 \mu m$) and 12 longwave (LW, $\lambda \geq 4\,\mu\text{m})$ spectral bands, making it well suited for various atmospheric conditions. The Fu-Liou model provides detailed insights into the interactions between cloud microphysics and radiation. The model vertical levels span the ground up to 10 km, with a greater density closer to the surface. In the first 100 m, the grid was spaced every 10 m and from 100 m to 1 km every 100 m. Input into the Fu-Liou model includes profiles of thermodynamic parameters, fog optical and microphysical quantities, aerosol optical properties, and surface reflectance and emissivity.

To perform simulations, the following specific data were provided to the model:

- T and specific humidity profile. The data from the soundings were combined with the sounding from Tarnów (WMO station 12575) more information is given in Appendix A.
- $r_{\rm eff}$. Due to limitations of the radiative transfer model, $r_{\rm eff}$ was assumed to be constant with height within the fog layer. It was calculated using data from the OPC-N3, which measures droplet concentrations in 24 size bins. To exclude aerosol particles, only bins 7 to 24 (corresponding to droplet diameters from 1.15 to 20 μm) were used in the calculation.
- Fog height. In the model it was assumed that the fog starts at the surface and reaches the CTH level. The top of the fog was determined as the point where $LWC < 0.12 \text{ g m}^{-3}$.
- Aerosol optical depth (AOD). Measurements from CIMEL at SolarAOT^{upper} were taken. To adjust how much the beam is weakened by the vertical distance between the upper and lower site, the value of AOD was added to the extinction coefficient (obtained from Aurora 4000 and AE-31) times the height difference (185 m) between both stations.
- Aerosol single scattering albedo (SSA). Based on AE-31 and Aurora 4000 located at SolarAOT^{upper}, the SSA was calculated. The value of SSA at the moment of the balloon sounding was obtained by linear interpolation.
- Aerosol Ångström exponent (AE) at 440/870 nm.
 A CIMEL sun photometer is installed at the SolarAOT^{upper} site. For the simulations, AE values were rounded to ensure consistent conditions across all cases. Data from both CIMEL and lidar indicate an influx of Saharan dust during the period of 8–10

- September. The approximate AE value recorded by CIMEL during these days was 0.5, increasing to 1.0 on 11 September.
- The asymmetry parameter was derived using Mie scattering theory. Initially, the liquid water content and effective droplet radius were employed to estimate the droplet number concentration, assuming a monodisperse size distribution. Subsequently, spectral optical properties extinction, scattering, and single scattering albedo were computed across relevant wavelengths. Finally, the asymmetry parameter was calculated by integrating the angular scattering phase function obtained from classical Mie theory.
- The model allows for the specification of surface albedo based on the International Geosphere-Biosphere Program (IGBP) land cover classification, using one of 20 predefined surface types. For all simulations performed in this study, the IGBP class was set to "grassland" (IGBP=10), as the measurement site was located on a valley slope predominantly covered with grass, with sparse one-family houses. Surface albedo was implemented as a spectrally resolved, solar zenith, and watervapor-content-dependent parameter.

4 Case study: valley of the city of Strzyżów

Fog was observed during three successive nights between 8 and 11 September 2023 in the valley of the city of Strzyżów. The balloon was launched after fog was visible at the lower station. Figure 5 presents the situation at the lower and upper stations during fog occurrence. Figure B2 presents photographs taken on 3 consecutive days at 04:00 UTC (all times in the paper are given in UTC unless specified otherwise) from the SolarAOT^{upper} station, showing the top of the fog layer. During the experiment, the fog was not detected at the upper site. Table 1 presents the duration of each fog event and its division into stages. In this section the evolution of each fog event will be described as well as its general pattern. The analyzed data are available for download from the Dane Badawcze UW repository (Nurowska, 2025).

4.1 Meteorological overview

The area of Poland, as well as almost all of Europe, was under the influence of anticyclonic circulation of high pressure from Russia. The pressure on 9 September was constant at 1019 hPa; from 09:00 UTC on 10 September it began to slowly drop to reach the value of 1012 hPa on 11 September at 11:00 UTC. During 8–10 September 2023, there was an event of Saharan dust over Poland. The AE measured for those days by CIMEL at SolarAOT^{upper} station was around 0.5 (for a period of Saharan dust) and 1.0 (for the morning of 11 September). The mean AOD during the dust episode

was not very high (0.19 at 500 nm). It can be seen from the lidar data (Fig. B1) that the sky was mostly cloudless. On 9 September in the morning, cirrus clouds were visible. The average wind speed did not exceed $2.5 \,\mathrm{m \, s^{-1}}$. Slow advection of hot air of tropical origin caused an inflow of Saharan mineral dust visible at 2-4 km a.g.l. on lidar data (Fig. B1). Figure 5d shows the aerosol scattering coefficient of light at 525 nm (ASC₅₂₅), for 3 nights of observations. On the night between 8-9 September 2023 ASC₅₂₅ was below 100 Mm⁻¹, which suggests moderate air quality conditions; just before the onset of fog at 21:30-22:30, the values peak to 240 Mm⁻¹, and after the end of fog, values once again peak exceed a very high level of 500 Mm⁻¹. These two peaks are probably due to industrial activity during inversion conditions and the turning on of the heating systems in houses. The morning peak is coincident with inversion disappearance and the transport of pollution from the bottom of the Strzyżów valley. On the night between 9 and 10 September ASC₅₂₅ descended during the night from 150 to 100 Mm⁻¹, with a peak to 250 Mm⁻¹ at 21:00 UTC. The cleanest conditions, with no evening peak of ASC₅₂₅, were on the night of 11 September, with values below 100 Mm⁻¹. At the upper station, always in the evening and at night, the values of ASC₅₂₅ were below 100 Mm⁻¹. The air in the valley was trapped under the inversion of temperature. The inversion formed at 18:00 at night from days 8 and 9 and around 19:00 at night on 10 September 2023. The course of T in the valley each day was similar during the day, reaching a maximum of 24–26 °C and reaching a minimum 12.5-13.5 °C around 05:00 UTC (Fig. 5). The inversion disappeared around 08:40, 07:40, and 08:10, respectively, for days 9, 10, and 11 September 2023. The RH at SolarAOT_{lower} station during fog reached 100 %. The air at SolarAOT^{upper} station was lower (RH = 60 %–90 %).

The lower panels of Fig. 5 show the calculated visibility in kilometers. Visibility was derived from ShadowGraph measurements using the Koschmieder formula, under the assumption of monodisperse droplets with a radius equal to the $r_{\rm eff}$ obtained from ShadowGraph, and LWC also provided by ShadowGraph data. An extinction coefficient of 2 was assumed, corresponding to the geometrical optics regime.

During the nights of 9 and 10 September, visibility decreased sharply around midnight, reaching values as low as 100–200 m. The fog dissipated abruptly around 06:00. In contrast, the fog event on the night of 11 September exhibited a different evolution: intermittent patches of fog began to form around midnight, followed by the development of a more continuous fog layer after 02:00, which persisted until approximately 06:00.

4.2 Fog microphysics

Based on OPC-N3 measurements, it was possible to compute LWC and LWP; results for each fog event are presented in Fig. 6. Observed fog mostly occurred in moderate aerosol conditions, and fog layers were located in the range of the

T inversion. The fog top varied from sounding to sounding; mostly it was 85 m (max. 115 m, see Fig 6).

Figures 7, 8, and 9 present the T and RH with height as well as LWC, N_c , and $r_{\rm eff}$ for each fog event. The profiles are shown starting from 2 m above the ground, as values below this height could have been significantly affected by surface influence or local disturbances during balloon launch procedures. For this reason, the lines fitted to the profiles were calculated from 2 m to 80% of the fog height. The level of 80% was chosen according to Cermak and Bendix (2011), that above 80% of the height, the fog layer mixes with the dry air above it, which contributes to the reduction of LWC. It is worth mentioning that at that stage of the year, the sunrise is at 04:00 UTC (local time 06:00). Time is given in UTC; for this period of year, UTC is -2 h from local time.

4.2.1 Thin-to-thick transition

In the observed fog events, several criteria were considered to identify a possible transition from thin to thick fog. Following Costabloz et al. (2025), we evaluated: IR net radiation at the surface, temperature, cloud top height, and liquid water path.

Costabloz et al. (2025) proposed five conditions to characterize this transition: (1) longwave net radiation approaches zero, (2) the temperature gradient between 50 and 25 m becomes negative, (3) TKE exceeds $0.10 \,\mathrm{m}^2 \,\mathrm{s}^{-2}$, (4) CTH exceeds $110 \,\mathrm{m}$, and (5) LWP exceeds $15 \,\mathrm{g} \,\mathrm{m}^{-2}$. They demonstrated that while all conditions were met for thick fog, the exact time when each was fulfilled could differ by up to 1 h, making precise estimation of the transition time challenging. In this study, we evaluated four out of five conditions proposed by Costabloz et al. (2025) (without the TKE condition). The following list outlines which criteria were met during each observed fog event.

- On the night of 8–9 September, the LWP exceeded 15 g m⁻² at 01:30. The IR net radiation criterion was satisfied for three profiles at 02:38, 03:48, and 04:16. The profile at 04:16 satisfied three out of the four criteria (IR net radiation, CTH, and LWP) and was conducted during a brief period of thicker fog just before sunrise. However, this state of thick fog did not persist for long.
- On the night of 9–10 September, the LWP exceeded 15 g m⁻² from the start of valid measurements at 02:30 until the fog dissipated.
- On the night of 10–11 September, the LWP exceeded 15 g m⁻² at 03:10, but the CTH did not reach the 110 m threshold.

Although the $15\,\mathrm{g\,m^{-2}}$ threshold suggested by Costabloz et al. (2025) was frequently exceeded, our results indicate that this value alone is insufficient to reliably distinguish

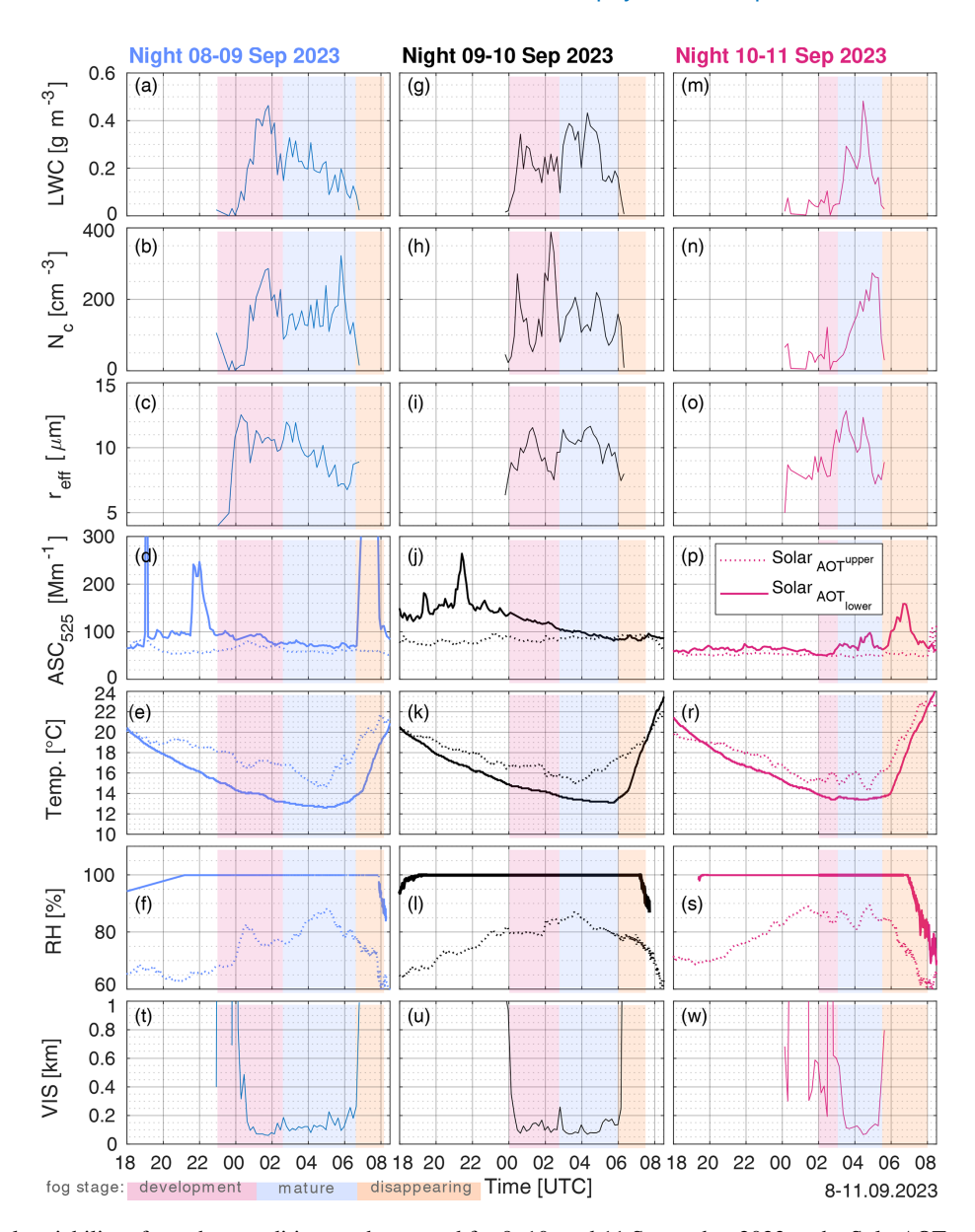


Figure 5. Temporal variability of weather condition on the ground for 9, 10, and 11 September 2023 at the SolarAOT_{lower} site (solid lines) and SolarAOT^{upper} station (dotted line). In panels (a), (g), and (m) LWC from ShadowGraph is presented; for reference, when the soundings of the balloon with installed OPC-N3 occurred, an overlay of Fig. 6 was added. Panels (b), (h), and (n) present the N_c of droplets registered by ShadowGraph. Panels (c), (i), and (o) show r_{eff} obtained from ShadowGraph. Panels (d), (j), and (p) present the ASC at 525 nm from Aurora 4000; panels (e), (k), and (r) T; panels (f), (l), and (s) RH; and panels (t), (u), and (w) visibility obtained from ShadowGraph.

between thin and thick fog. Therefore, we interpret the fog event on 9 September as a case in which a transition towards thick fog had started but was interrupted by sunrise before full development. In the fog events on 10 and 11 September, the other criteria were not met. In none of these cases did the LWP exceed $30\,\mathrm{g}\,\mathrm{m}^{-2}$ – the threshold for thick fog proposed by Wærsted et al. (2017). Given that the period of thick fog was very short-lived and most observations remained within the thin fog regime, our findings should be considered primarily representative of optically thin fog conditions.

4.2.2 Night of 8–9 September 2023

The fog event during the night of 8–9 September 2023 was observed from its development stage (23:00–01:41) through its mature stage (02:45–06:42) until dissipation (06:45–07:00). Figure 7 presents vertical profiles of microphysical parameters, including LWC, $N_{\rm c}$, and $r_{\rm eff}$, along with T and RH. The equivalent adiabaticity ($\alpha_{\rm eq}$) is shown in the figures displaying LWC profiles. The division into fog life cycle stages is illustrated in Fig. 7 by pink, blue, and yellow ochre corresponding to the development, mature, and dissi-

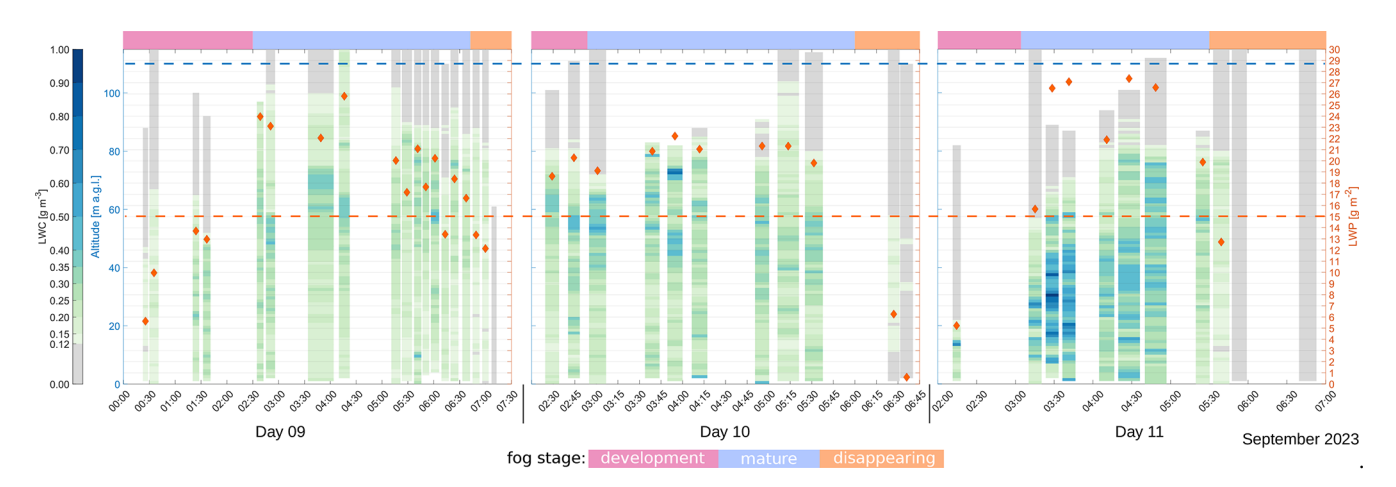


Figure 6. The bar chart with green-blue colors indicates the change in time of fog LWC with height for days (a) 9, (b) 10, and (c) 11 September 2023. The left axis represents the height, while the right axis corresponds to the total LWP for each balloon sounding (marked by an orange diamond). Blue dashed line indicates the 110 m, and orange line indicates LWP equal to 15 g m⁻². These are criteria indicating the transition from thin to thick fog by Costabloz et al. (2025)

pation stages, respectively. Apart from that, separate figures can be found in the Appendix for each stage: Figs. B3a and b and B4. Each of the fog stages is described below.

- Development of fog. There were five soundings conducted between 23:00-02:34 (see Fig. B3a). T decreased with height from the ground to 40 m a.g.l., starting from T = 12.0 °C and decreasing at the rate $\gamma_{\rm fit} \cdot \Gamma_{\rm wa} = 0.48 \cdot (-5.0) \,{}^{\circ}{\rm C\,km}^{-1}$. Above 40 m, a temperature inversion was present, with T reaching 14.7 °C at 100 m. The top of the fog was 65 m. The RH was constant, equal to 100% up to 87m, and in the last 10 m it dropped with height (96 % at 100 m). LWC slightly increased with height ($\alpha_{\rm fit} \cdot \Gamma_{\rm ad} =$ $1.34 \cdot 2.32 \,\mathrm{g} \,\mathrm{m}^{-3} \,\mathrm{km}^{-1}$), from 0.18 to a maximum of $0.30\,\mathrm{g\,m^{-3}}$ at 23 m a.g.l.; up to 36 m a.g.l., LWC was oscillating near $0.26\,\mathrm{g\,m^{-3}}$, and above that it decreased. α_{eq} was 0.29. LWC_{ShadowGraph} (referring to LWC measured by the ShadowGraph, Fig. 5) shows that during the development stage, LWC_{ShadowGraph} increased, reaching its maximum of $0.46 \,\mathrm{g}\,\mathrm{m}^{-3}$ at 01:47. Values of LWC from ShadowGraph were higher than those from OPC-N3. LWP (Fig. 6) increased from $5.63 \,\mathrm{g}\,\mathrm{m}^{-2}$ at 00:25 to 12.97 g m⁻² at 01:36. Mean $N_{\rm c}$ increased with height to 247 cm⁻³ at 35 m and then decreased with height to 48 cm⁻³ at 65 m. $r_{\rm eff}$ decreased steadily with height from 11.2 to 5.7 µm at the CTH.
- *Mature state of fog.* There were 13 soundings conducted from 02:34 till 06:42 (Fig. B3b). T and RH showed a similar pattern to height, as in the previous stage. The fog was deeper, with a top at 102 m. However, the temperature inversion started higher, around 60 m above the ground, and the lapse rate in the lower part was higher: $\gamma_{\rm fit} \cdot \Gamma_{\rm wa} = 1.16 \cdot (-5.1) \,^{\circ}{\rm C \, km^{-1}}$. The

 $N_{\rm c}$ maximum, equal to $410\,{\rm cm}^{-3}$, was at 48 m; above this, $N_{\rm c}$ decreased to 65 cm⁻³ at 90 m. Above that, the number of drops was constant. The $r_{\rm eff}$ profile changed and can be divided into two sections. From the ground to a height of 88 m, $r_{\rm eff}$ remained almost constant (at bottom 9.2 µm; 8.3 µm at 88 m). From 88 m to CTH, $r_{\rm eff}$ decreased sharply with height (mean at the top 5.2 µm). Because the $N_{\rm c}$ maximum is shifted upward, the LWC maximum is also at a higher altitude (56 m). The $\alpha_{\rm fit}$ is positive, equal to 0.90, and $\alpha_{\rm eq}$ is equal to 0.30. The images from the ShadowGraph indicate that LWC_{ShadowGraph} near the ground decreased over time starting from 2:57, and this was associated with a decrease in $r_{\rm eff}$ and not $N_{\rm c}$.

- Disappearing stage. There were two soundings conducted between 06:45 and 07:00 (Fig. B4). T increased from the ground to 27 m, above which T decreased with height. Unfortunately, the sounding with the Vaisala radiosonde RS41 was interrupted at 45 m. Between the two soundings, spaced less than 15 min apart, the T profile shifted by +2 °C. At this time, the RH profile dropped by 5%. In the first 20m, the mean RH dropped from 96 % near the ground to 91 % at 20 m. The fog evaporated quickly. The α_{eq} was positive, equal to 0.33. LWC increased with height $(\alpha_{\rm fit} \cdot \Gamma_{\rm ad} = 0.42 \cdot$ $2.39\,\mathrm{g\,m^{-3}\,km^{-1}}$), reaching a maximum at 72 m (mean LWC $0.26 \,\mathrm{g}\,\mathrm{m}^{-3}$); at almost the same height, $N_{\rm c}$ also reached its maximum (488 cm⁻³ at 74 m). The layer above was characterized by a rapid decrease in both values up to the CTH. The $r_{\rm eff}$ was constant with height up to 80 m, around 6.8 µm, except for the layer from the ground to 18 m, where $r_{\rm eff}$ was higher, up to 9.5 μ m.

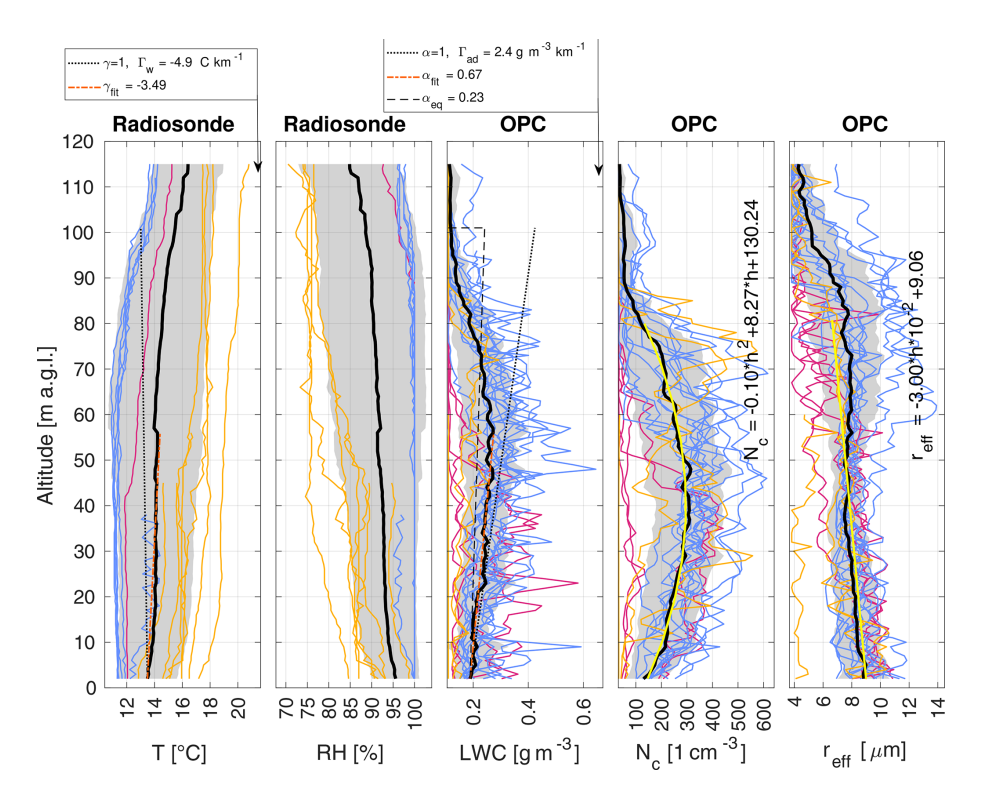


Figure 7. Vertical profiles of specific quantities measured by the balloon for the night of 8–9 September 2023. From left: T and RH from Vaisala radiosonde RS41, LWC, N_c , and r_{eff} within the fog from OPC-N3. Each colored line represents an individual balloon profile, with different colors indicating different stages of fog evolution: pink corresponds to the formation stage, blue to the mature stage, and yellow ochre to the dissipation stage. The black thick line represents the mean of all the soundings, and the colored area represents the range between ± standard deviation from the mean. In the T plot, the dotted line presents the wet adiabatic lapse rate Γ_W , and the dashed red line presents linear fit of T from 2 m to height of maximum mean LWC. γ_{fit} is a scaling factor of Γ_W to obtain the equation of linear fit. In the LWC plot, the dotted line presents the LWC adiabatic lapse rate Γ_{ad} , and the dashed red line presents the linear fit to LWC from 2 m to the height of maximum mean LWC. α_{fit} is a scaling factor of Γ_{ad} obtained by fitting line to LWC dependence from height, and α_{eq} is a scaling of Γ_{ad} , which would give the same LWP for the whole cloud/fog. In the N_c plot, the yellow line indicates the quadratic fit to the data (from 2 m to 80 % height of CTH). In the r_{eff} plot, the yellow line indicates the linear fit to the data (from 2 m to 80 % height of CTH).

Figure 7 presents the mean values with height for the whole-night fog event from 8–9 September 2023. For the entire fog event, $\alpha_{\rm eq}$ is 0.23. As a first approximation, fog $r_{\rm eff}$ decreases linearly with height, while $N_{\rm c}$ can be approximated by a quadratic equation. The equations for fitted lines are, respectively,

$$r_{\text{eff}} = 0.03 \cdot h + 9.06 \,[\mu\text{m}],$$
 (11)

$$N_{\rm c} = -0.10 \cdot h^2 \cdot 10 + 8.27 \cdot h + 130.24 \,[\text{cm}^{-3}]. \tag{12}$$

4.2.3 Night of 9–10 September 2023

Below are described the stages of fog from 9–10 September 2023:

Development of fog. Due to a malfunction of the apparatus, the development stage of fog with microphysics measurements in the vertical direction was not captured. The fog started at 00:00; however, it is

not possible to determine when this stage ended. The first OPC-N3 sounding was registered at 02:34, with LWP $> 15 \, \mathrm{g \, m^{-2}}$.

Based on ShadowGraph measurements, LWC and $N_{\rm c}$ increased continuously until 00:37, reaching local maxima: LWC_{ShadowGraph} = 0.34 g m⁻³ and $N_{\rm c} = 271 \, {\rm cm}^{-3}$. The $r_{\rm eff}$ reached its local maximum later, at 01:17, equal to 11.6 µm. After the peak, values of LWC, $N_{\rm c}$, and $r_{\rm eff}$ fluctuated, reaching their global maxima ($N_{\rm c} = 388 \, {\rm cm}^{-3}$ at 02:18) and minima ($r_{\rm eff} = 7.5 \, {\rm \mu m}$ at 02:28).

Two profiles of T and RH are shown in Fig. B5a. The profile reaching a higher altitude was performed earlier, at 00:53, and the second about 1 h later. The temperature profile was nearly constant in the first 40 m (12.65 °C at the ground), above which a temperature inversion was present that weakened with time. The RH was 100 % up to 67 m and then decreased with height. RH was con-

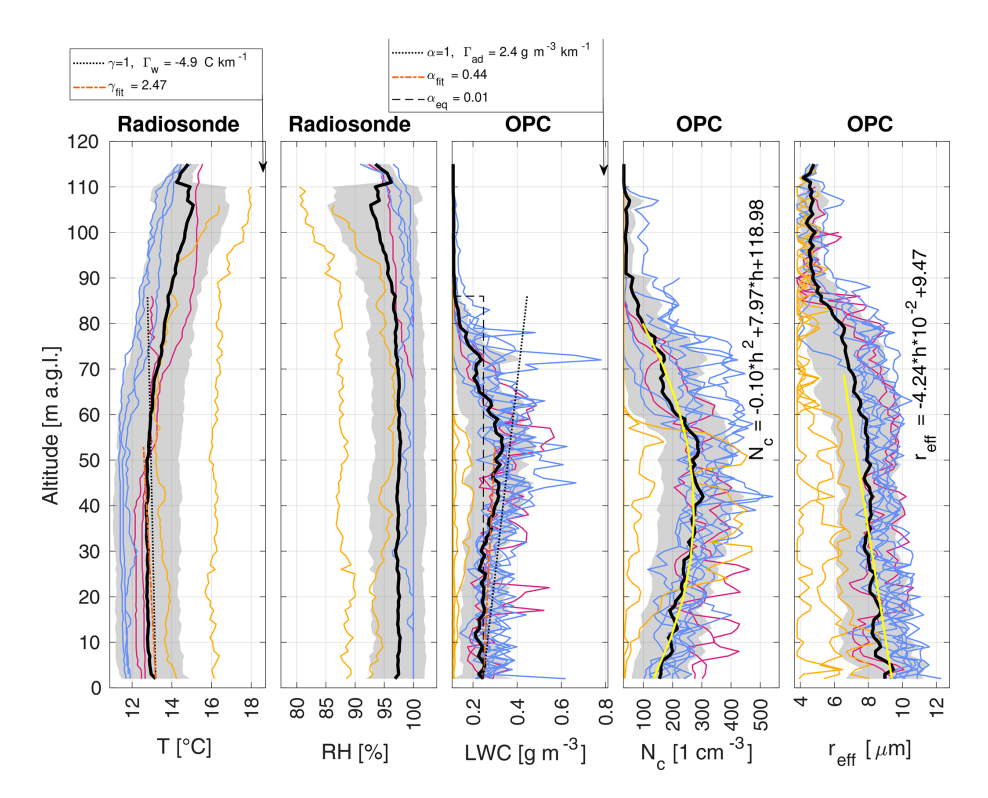


Figure 8. Vertical profiles of specific quantities measured by the balloon for the night of 9–10 September 2023. A detailed description is given in the caption of Fig. 7.

stant at 100% throughout the entire column from the ground up to 86 m 1 h later.

- Mature state of fog. There were 13 soundings conducted from 02:45 to 06:42 (Fig. B5b). The fog height was 87 m. The temperature decreased with height up to 50 m a.g.l., above which a temperature inversion occurred. From the ground to the CTH, RH remained above 99.5 %. The maximum LWC was observed at 53 m, with a value of 0.40 g m⁻³.

A linear fit to the LWC profile from 2 to 53 m yielded a growth rate equal to 0.51 of the LWC adiabatic lapse rate. The maximum $N_{\rm c}$ was lower than during the previous night, reaching 345 cm⁻³. The $r_{\rm eff}$ at the ground was higher than in the previous day's fog; however, it decreased with height in the first 30 m, remained approximately constant (9.0 µm) from 30 to 63 m, and then decreased again toward the CTH.

The LWP (Fig. 6) oscillated between 18 and 23 g m $^{-2}$. Most of the water was located in the upper part of the fog, between 30 and 70 m.

Disappearing stage. Five soundings were conducted between 06:30 and 07:30 (Fig. B6). The temperature at 2 m a.g.l. and throughout the column increased rapidly (from 11.9 °C at 06:30 to 16.22 °C at 07:30). In the first 54 m, T decreased with height, and above this level, a

temperature inversion was observed. As the sun rose, RH decreased from 100 % to 88 % at 2 m a.g.l.

The parameters $\alpha_{\rm fit}$ and $\alpha_{\rm eq}$ were 0.30 and 0.24, respectively. LWC values were below 0.12 g m⁻³ in the first 21 m above the ground. The maximum LWC (0.15 g m⁻³) occurred at 43 m. When fog almost dissipated (06:23; Fig. 6), remaining fog patches were still observed between 30 and 50 m, with LWC > 0.15 g m⁻³. The fog top dropped to 57 m.

Fog droplet diameter decreased with height from $6.7 \, \mu m$ at $4 \, m$ a.g.l. to $4.8 \, \mu m$ at the CTH. N_c fluctuated around $170 \, cm^{-3}$ between 24 and 56 m. The fog dissipated from both the top and bottom.

The temperature in the first 53 m was almost constant with height. Within this layer, LWC increased with height at a rate of $\alpha_{fit} \cdot \Gamma_{ad} = 0.44 \cdot 2.4 \, g \, m^{-3} \, km^{-1}$, reaching a local maximum of LWC = 0.33 g m $^{-3}$ at 53 m. The corresponding value of α_{eq} was nearly zero (0.01).

Figure 8 summarizes the microphysical properties of the fog event on 9–10 September 2023. The following curves were fitted to the values of N_c and $r_{\rm eff}$:

$$N_{\rm c} = -0.10 \cdot h^2 \cdot 10 + 7.97 \cdot h + 118.98 \,[{\rm cm}^{-3}],$$
 (13)

$$r_{\text{eff}} = 4.29 \cdot h \cdot 10^{-2} + 9.47 \,[\mu\text{m}].$$
 (14)

4.2.4 Night of 10-11 September 2023

The fog pattern on the night of 10–11 September looks distinct from previous nights. The fog could not form until 03:08, when it started to develop with an abrupt jump in LWC from 0.05 at 03:08 to 0.30 at 03:31. The maximum peak in LWC observed on the ground by ShadowGraph was at 04:27, equal to 0.48 g m $^{-3}$. Fog rapidly intensified, reaching high LWC values (mean 0.48 g m $^{-3}$) in the fog body from 10–50 m, with maximum LWC 0.97 g m $^{-3}$ at 31 m at 03:23. At 04:40, high values of LWC above 0.40 g m $^{-3}$ were distributed in the range from the fog bottom to 80 m. As quickly as it appeared, the fog dissipated by 05:40. However, as before, the fog dissipated more from the bottom than from the top.

During the night of 10–11 September 2023, all stages of fog were captured; each stage is described in detail below. This fog event developed later in the night than previous cases and exhibited more abrupt behavior.

- Development of fog. Between midnight and 02:28, the ShadowGraph detected droplets; however, the LWC_{ShadowGraph} was below 0.1 g m⁻³. Two soundings were performed, one with OPC-N3 and one with the Vaisala radiosonde RS41, between 02:00 and 03:02 (Fig. B7a). The profile from 02:11 shows that the fog was just forming. LWP was 5.23 g m⁻².

Fog was confined to the first 23 m in height. Even though the fog was shallow, it had high LWC values at some levels (max. LWC was 0.67 g m⁻³ at 13 m). The $\alpha_{\rm eq} = -3.22$; however $\alpha_{\rm fit} = -0.15$.

The fog was dense; the maximum $N_{\rm c}$ was 416 cm⁻³ at 18 m. The $r_{\rm eff}$ decreased with height (9.8 μ m at 2 m and 6.0 μ m at the CTH). The profile from the Vaisala radiosonde RS41 at 02:43 shows that T remained almost constant in the first 40 m (around 12.7–12.8 °C), later slightly increasing with height to 14.2 °C at 100 m.

The RH profile was constant with height; however, the air was not fully saturated (RH \approx 98.5%). ShadowGraph shows that LWC dropped to 0 at 02:38 and within the next hour rapidly rebuilt to 0.30 g m⁻³. This was correlated with rapid growth of $r_{\rm eff}$ from 7.8 μ m to 12.8 μ m, while $N_{\rm c}$ remained low (2–65 cm⁻³).

Mature state of fog. Between 03:10 and 05:30, eight soundings with a balloon (Fig. B7b) were conducted.
 The fog deepened to 83 m. The profiles of T and RH changed: only in the first 10 m was RH above 99.5%, above which it decreased to 85.5% at 60 m.

Unfortunately, the sounding with the Vaisala radiosonde RS41 did not reach the CTH. There was a strong inversion; the fitted lapse rate was $\gamma_{\rm fit} \cdot \Gamma_{\rm wa} = -11.82 \cdot -4.97\,^{\circ}{\rm C~km}^{-1}$. T increased from 12.3 $^{\circ}{\rm C}$ at the ground to 15.8 $^{\circ}{\rm C}$ at 60 m.

The $N_{\rm c}$ profile had a different form compared to previous fog events: it exhibited two protrusions with maxima at 25 m (377 cm⁻³) and 70 m (257 cm⁻³) and a local minimum at 50 m. The $r_{\rm eff}$ slightly decreased from the ground (10.0 μ m) to 60 m (8.8 μ m) and then decreased more sharply to 5.5 μ m at the CTH.

The LWC profile showed a more intermittent pattern, with values fluctuating between 0.2 and 1.2 g m⁻³ and a peak of 0.67 g m⁻³ at 27 m. $\alpha_{\rm eq} = 0.56$, and fitted $\alpha_{\rm fit} = 4.80$. The LWP was the highest of all three events; for four soundings, LWP exceeded 26.5 g m⁻² (maximum: 27.36 g m⁻² at 04:27).

Disappearing stage. The final stage of fog was observed from 05:30 to 06:00. Two soundings were conducted with OPC-N3. In Fig. B8, two additional soundings of T and RH between 06:00 and 06:33 are also shown. The CTH was at 79 m.

LWC increased with height, with a maximum near the CTH (max. LWC = $0.19 \, \mathrm{g \, m^{-3}}$ at 75 m). Due to the location of the maximum LWC near the CTH, $\alpha_{eq} = 0.32$, which was similar to $\alpha_{fit} = 0.30$.

 $N_{\rm c}$ increased with height to 27 m (maximum 190 cm⁻³), then oscillated around 145 cm⁻³ up to 43 m, and then sharply decreased to 62 cm⁻³ at 48 m. The $r_{\rm eff}$ slightly decreased with height, with fluctuations around 6 μ m.

Figure 9 summarizes the microphysical properties of the fog event on 10–11 September 2023. α_{eq} for the entire event was 0.24. The following curves were fitted to the values of N_c and r_{eff} :

$$N_{\rm c} = -0.04 \cdot h^2 + 1.47 \cdot h + 219.65 \,[{\rm cm}^{-3}],$$
 (15)

$$r_{\text{eff}} = 4.61 \cdot h \cdot 10^{-2} + 9.57 \,[\mu\text{m}].$$
 (16)

4.3 Evolution of fog droplet spectrum

From the OPC-N3 measurements, it was possible to compute vDSD(r) presented in Fig. 11a. vDSD is presented from bins of radius from 1.15 to 20 μ m to remove aerosol particles. ShadowGraph was located near the ground; Fig. 10 presents the comparison between the vDSD obtained from ShadowGraph and OPC-N3. ShadowGraph shows that near the ground, there are droplets of radius greater than 20 μ m and that in the case of OPC-N3, those droplets are counted in the last bin. As was stated by Nurowska et al. (2023), even though the manufacturer declares that the upper limit of the last bin is 20 μ m, in fact, the last bin also counts larger particles.

Although OPC-N3 is not calibrated to match the vDSD values, it has a similar pattern of spectrum as ShadowGraph. The vertical profile of the vDSD (Fig. 11a) provides information on which droplet sizes contribute most to the LWC at

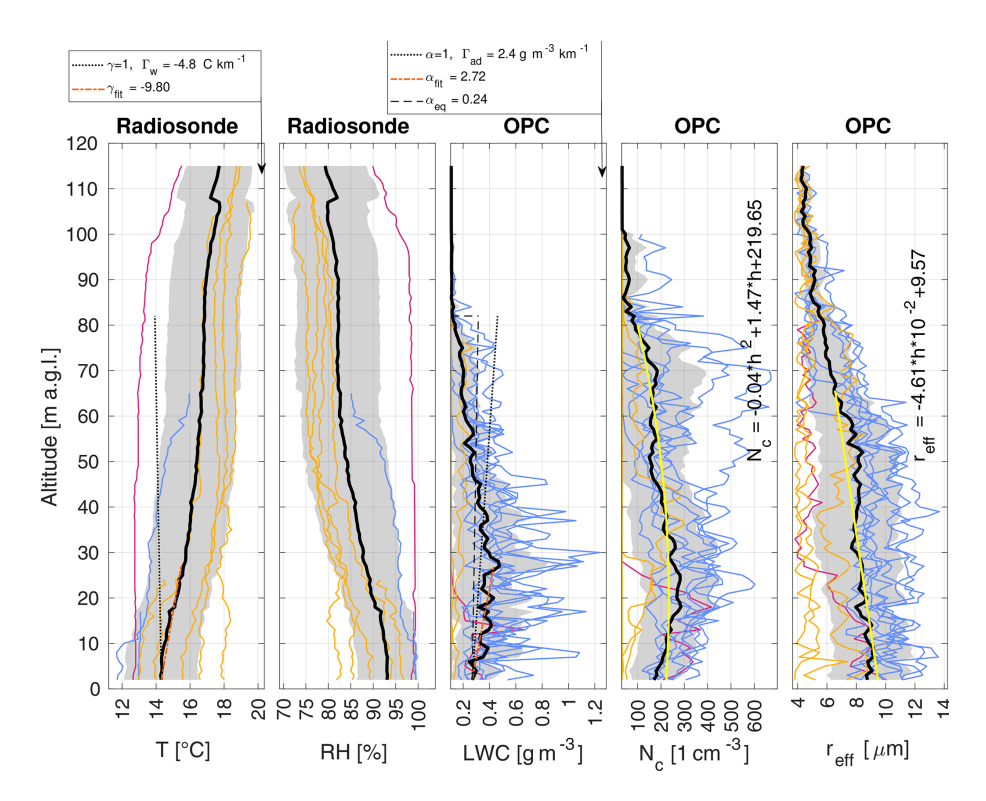


Figure 9. Vertical profiles of specific quantities measured by the balloon for the night of 10–11 September 2023. A detailed description is given in the caption of Fig. 7.

a given height. Figure 11b shows the normalized vDSD, obtained by dividing the droplet size distribution at each height by $\sum_{r_b} \text{vDSD}(r_b)$ at that height. This normalization highlights the relative contribution of each size bin to the vDSD at a given altitude.

Figure 11a indicates the altitudes where most LWC is produced and by which droplet sizes, while Fig. 11b enables analysis of the droplet spectrum in regions with low LWC – such as near the top of the fog layer or during dissipation. Apart from vDSD for the whole episode, in the Appendix (Fig. B9), vDSD is shown for each stage of fog: beginning, mature, and disappearing. This section describes how LWC, LWP, and the droplet spectrum evolve during fog occurrence for each night case.

From vDSD (Fig. 11) it is visible that most of the LWC is associated with two drop radius regions. The first region is described by an asymmetric distribution. The maximum value of the distribution is associated with a radius of 4–5 μ m. The distribution has a bigger slope on the left side (droplets smaller than the maximum). The second region is a peak for droplets of radius bigger than 18.5 μ m ($r_{>18.5}$). Big droplets are found in the whole range of altitudes; however, there are more of them when closer to the ground.

In the 10 m layer closest to the ground, droplets with $r > 18.5 \,\mu\text{m}$ contribute up to 40 % of the total LWC. Within this layer, the closer to the surface, the smaller the contribu-

tion to LWC from droplets with $r < 7 \,\mu\text{m}$ and the larger the contribution from droplets with $r > 7 \,\mu\text{m}$.

Above 10 m, the situation is reversed: droplets with $r < 7 \, \mu \text{m}$ contribute more to LWC than those with $7 \, \mu \text{m} < r < 18.5 \, \mu \text{m}$. Above 40 m, with increasing altitude, the 4–5 μ m peak in the normalized vDSD gradually shifts toward larger droplet sizes, reaching approximately 8–9 μ m.

The maximum CTH during fog on 9 September was approximately 102 m. In most cases, the LWC above 80 m was below $0.2\,\mathrm{g\,m^{-3}}$, indicating only sparse droplets in this region. Just above the CTH, most of the water was accumulated in droplets with radii between 8 and $14\,\mu\mathrm{m}$. With increasing height, this droplet size range decreased.

Subsequent fog nights had increasingly larger LWC at a specific height (see Fig. 6). Even though LWC reached higher values on 10 September than on 9 September, the LWP was higher on 9 September because the fog was reaching higher altitudes. The increase in LWC was related to the appearance of droplets in the size of 7–17 μm and not to the increase in the number of droplets in the size of 4–5 μm .

In the Appendix, Fig. B9 presents vDSD for three stages of fog for each day. Even in the initial stage of the fog, there were already large drops with $r_{>18.5}$, and the fog started to grow in thickness from the bottom. In the case of the fog from the nights of 9 and 10 September, with increasing height, water was stored by drops with increasingly larger radii between $2-10\,\mu\text{m}$. In the case of the fog from the night of 10

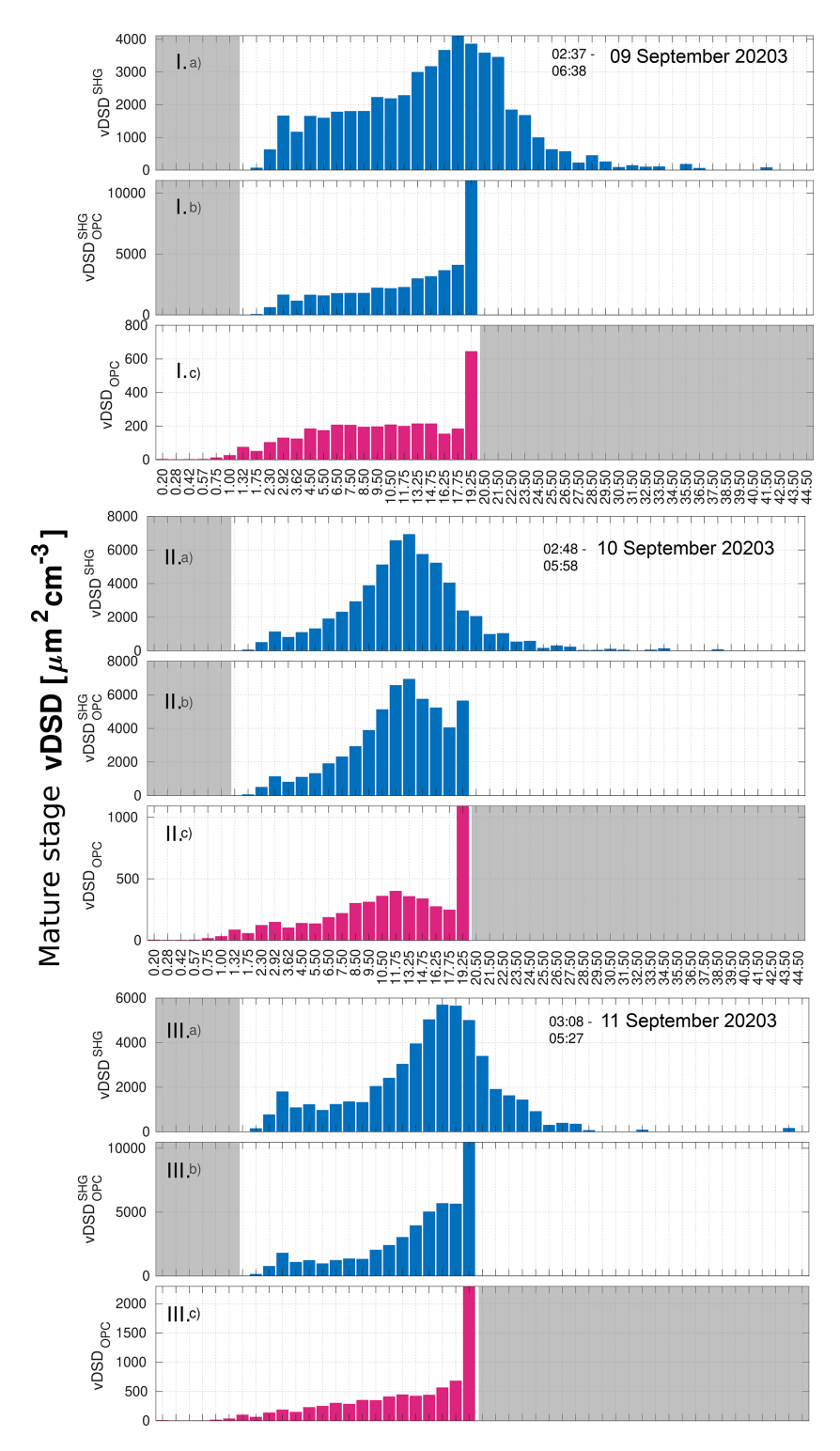


Figure 10. vDSD near ground for mature stage of night events of fog on (I) 8–9 September, (II) 9–10 September, and (III) 10-11 September 2023. Panels (**a**) and (**b**) present the vDSD obtained from Shadowgraph, while (**c**) presents vDSD from OPC-N3. The *x* axis represents the edges of the bins of droplet radii measured by OPC-N3 and additionally greater bins (above 20 μm) visible only by Shadowgraph. Panel (**b**) presents the same vDSD as panel (**a**); however all the droplets with radius greater than 20 μm are counted as part of the last bin of OPC-N3 (18.5–20 μm) – this is done to be able to compare the vDSD from OPC-N3 and Shadowgraph. The imaging area for a given device is marked in white.

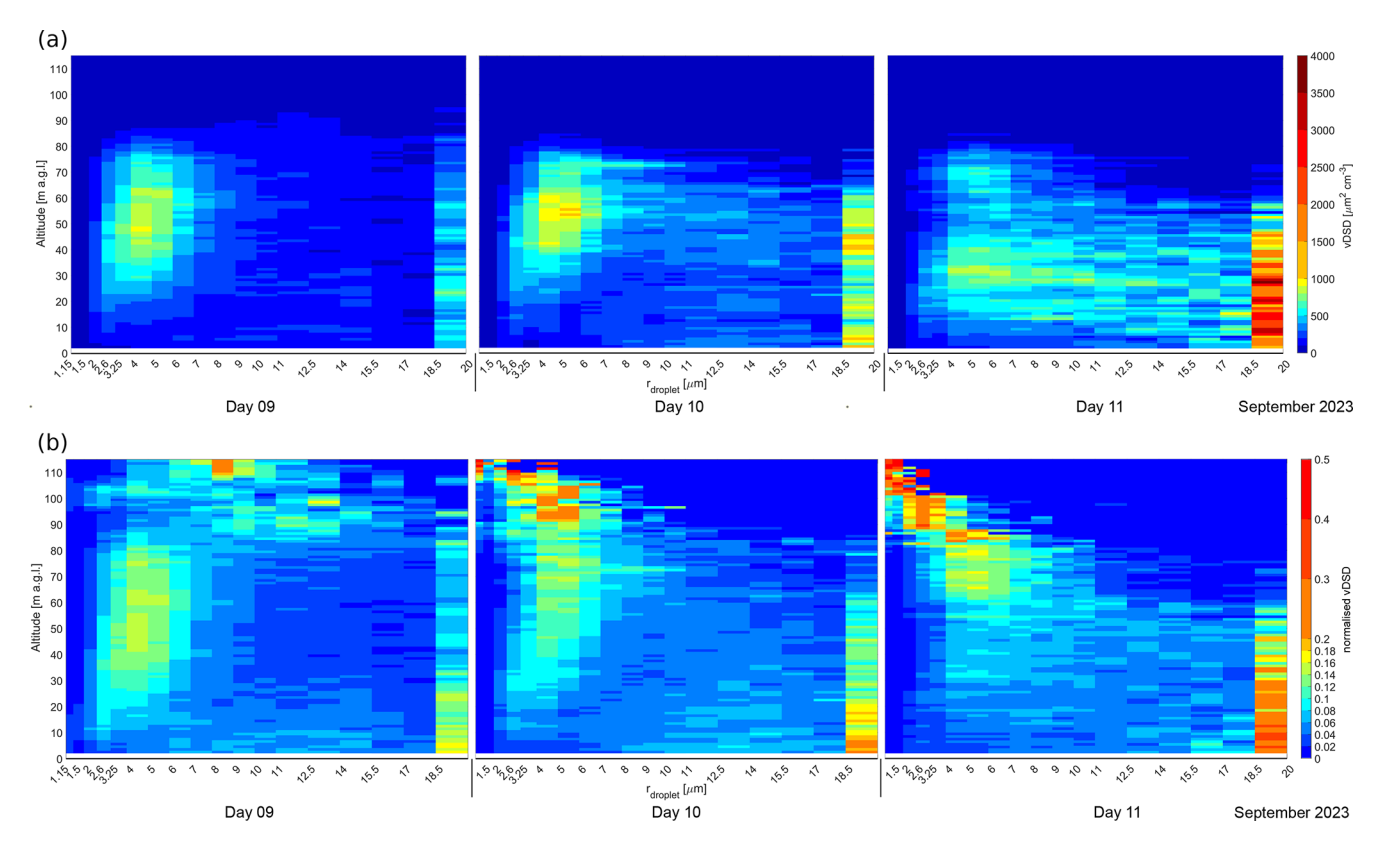


Figure 11. Vertical profile of vDSD and normalized vDSD for 9–11 September 2023 fog occurrence. Panel (a) presents the vDSD. The scale is divided into steps of $100 \, \mu m^2 \, cm^{-3}$ from 0 to $1000 \, \mu m^2 \, cm^{-3}$ and then in steps of $500 \, \mu m^2 \, cm^{-3}$. Panel (b) presents the normalized at each height vDSD. The figure presents what percentage of the entire spectrum at a given height is contributed by the volume of drops from a given bin.

to 11 September, with increasing height, an inverse relationship occurs – increasingly smaller drops store the most water from the range of radii $2.0{\text -}18.5\,\mu\text{m}$.

In the dissipating stage of fog on 9 and 11 September, the CTH did not decrease; it remained around 80 m, while below 30 m, the vDSD shows minimal signal (bottom panels of Fig. B9), suggesting a very low droplet concentration in this region. This suggests that the fog disappeared more from the bottom than from the top.

As the profile of the dissipating fog on 10 September was taken approximately half an hour after the dissipation began, it captured only small droplets in the range of $2-7 \,\mu m$ at heights between 20 and 60 m. In all cases, large droplets $(r_{>18.5})$ ceased to contribute significantly to the LWC during the fog dissipation phase.

4.4 Optical, microphysical, and radiation closure

A radiative closure was performed to assess the consistency between observed radiative fluxes and the microphysical measurements. Given that the OPC-N3 is a low-cost optical particle counter, we wanted to verify whether the vertical profiles of microphysical parameters were representative of actual conditions. Since no independent method was available, we used the obtained microphysical parameters as input for radiative transfer simulations. These simulations enabled us to test whether the microphysical measurements from the OPC-N3 are consistent with the observed radiative fluxes.

Radiative transfer simulations were conducted using the Fu–Liou model in 1D mode, incorporating detailed vertical profiles of thermodynamic and microphysical properties. The model covers 6 shortwave and 12 longwave spectral bands, with input data including fog microphysics, aerosol optical properties, and surface reflectance. The fog droplet asymmetry parameter was calculated using Mie theory, based on measurements of liquid water content and droplet size. Details of the model setup are provided in Sect. 3.4.

For performing the simulations, only cases in which setup 1 (with OPC-N3) was attached to the balloon and data were properly collected were used. The simulated shortwave (SW) and longwave (LW) fluxes were compared with fluxes registered at the SolarAOT^{upper} and SolarAOT_{lower} stations. Two flights on 11 September between 05:40 and 06:22 were excluded from the radiative closure analysis due to suspected water condensation on the lower LW radiometer during fog

dissipation. In total, there were 37 soundings used for analysis

Figure 12 compares SW and LW radiation between the model and observations at the SolarAOT^{upper} and SolarAOT_{lower} stations. The scatter plots also show linear fits to the data. The left panels present the model results for clear-sky conditions based on observations from 10 September, while the right panels present results from the time when there were fog conditions during days 9–11 September.

Upper-air temperature and humidity profiles were taken from balloon soundings by the Polish Meteorological and Water Management Institute in Tarnów, available only twice daily (00:00 and 12:00 UTC), resulting in limited temporal resolution above 100 m. In contrast, near-surface profiles were measured more frequently on site (when fog was present). Therefore, for comparison of clear-sky conditions, only data from near the sounding at $12 \pm 2 \, h$ were used.

The equation describing the relationship between the SW radiation under clear-sky and fog conditions for both stations has a relation of almost 1: 1. The offset is up to -12 W m^{-2} .

Given the limited variation in LW downward radiation and the uncertainties introduced by sparse temperature soundings, absolute comparisons via regression provide limited insight. Instead of separate scatter plots for two stations, we present the difference in LW radiation between the upper and lower stations. The offset of the linear fit by $13.10\,\mathrm{W\,m^{-2}}$ suggests that the fog implemented in the model can be too thick.

Figures 13 and 14 show the temporal comparison of SW and LW fluxes between the model and observations at the SolarAOT^{upper} and SolarAOT_{lower} stations. Black lines show the measured incoming SW and incoming LW radiation fluxes. The simulation result for clear-sky conditions is presented by the yellow dashed line, while the orange circles present the result of the simulation with implemented fog conditions, based on soundings. The difference between observations and the model is shown in Fig. 14 in the lower panel for LW flux and in Fig. 13 in the second panel from bottom for SW flux. Additionally, Table 2 presents the statistics between simulated and measured SW and LW flux for clear-sky (no fog) and fog conditions.

For clear-sky SW radiation, the model flux at the SolarAOT^{upper} station is underestimated. The root mean square error (RMSE) for 9 and 10 September is 25.7 and 5.4 m⁻², respectively. On 9 September, the SW radiation at the SolarAOT^{upper} station exhibits a rugged temporal pattern due to the presence of cirrus clouds. The relatively high RMSE on this day is attributed to cirrus cloud contamination, which was not accounted for in the radiative transfer model. For the SolarAOT_{lower} station, the RMSE is 23.1 and 10.5 W m⁻², respectively, for 9 and 10 September.

The model LW flux at both sites for clear-sky conditions is underestimated, and the RMSE exceeds $30\,\mathrm{W}\,\mathrm{m}^{-2}$ for the upper station. Running the model based solely on aerological soundings performed twice daily does not allow for an

accurate representation of the diurnal variation of LW radiation. The results show significant discrepancies between the model and observations at both the upper and lower stations. To better reproduce the temporal evolution of IR radiation, more detailed information on the distribution of RH in the lower atmospheric layer is required.

The results indicate that when fog conditions are included, the model reproduces both SW and LW fluxes reasonably well at both stations. This is due to inputting more information from our soundings. For the SolarAOT^{upper} station, SW fluxes are slightly overestimated (by up to $12.7 \, \mathrm{W \, m^{-2}}$), while LW fluxes show deviations within $\pm 4 \, \mathrm{W \, m^{-2}}$.

At the SolarAOT_{lower} station, biases for both SW and LW fluxes remain within $12.2 \, \text{W m}^{-2}$. The RMSE generally stays below 14.2 W m⁻², except under cirrus cloud conditions (9 September). The RMSE values for LW radiation at the lower station are approximately 12–13.5 W m⁻² during fog conditions, indicating that the chosen fog microphysical parameters – liquid water content LWP and $r_{\rm eff}$ – adequately represent the fog's thermal radiative properties. The relatively low deviation suggests that the modeled fog layer produces realistic LW fluxes near the surface, supporting the suitability of the microphysical assumptions for the observed conditions. Due to model simplifications, the fog is assumed to have a constant droplet size and LWC at all heights, which may introduce some uncertainty into the results. As can be seen from the temporal comparison of LW radiation from model and data (Fig. 14), most of the model overestimation occurs during the fog decay stage; these errors may result from the lack of homogeneity or the patchwork nature of the fog during its decay. Overall, these results demonstrate that the model captures the radiative fluxes with acceptable accuracy during fog events.

4.5 Radiative fluxes during fog events

The apparatus at SolarAOTupper and SolarAOTlower station measures the total net radiation (NET; downward – upward SW + LW fluxes), which is presented in the lowest panel of Fig. 13. During the first night of observations, it is visible that between 00:00 and 00:44 the NET radiation at the SolarAOT_{lower} station changed from -24.4 to $-6 \,\mathrm{W}\,\mathrm{m}^{-2}$. After the development of fog, the NET radiation at the lower station was around 0 W m⁻². It became positive after sunrise. The difference between lower and upper station NET radiation during night fog was around $50 \,\mathrm{W}\,\mathrm{m}^{-2}$. When the fog disappeared (07:00), there was a visible abrupt jump of 156 W m⁻² at the lower station within 15 min. For the night of 9-10 September 2023, the fog also started to develop around midnight (at 00:50 the NET radiation was −5.8 W m⁻²). NET radiation at SolarAOT_{lower} became positive after sunrise, and a jump of $134 \,\mathrm{W}\,\mathrm{m}^{-2}$ occurred at the moment of fog disappearance at 06:20–06:40.

During the last night of observations, the NET radiation at the lower station was -44 W m^{-2} at midnight, while at the

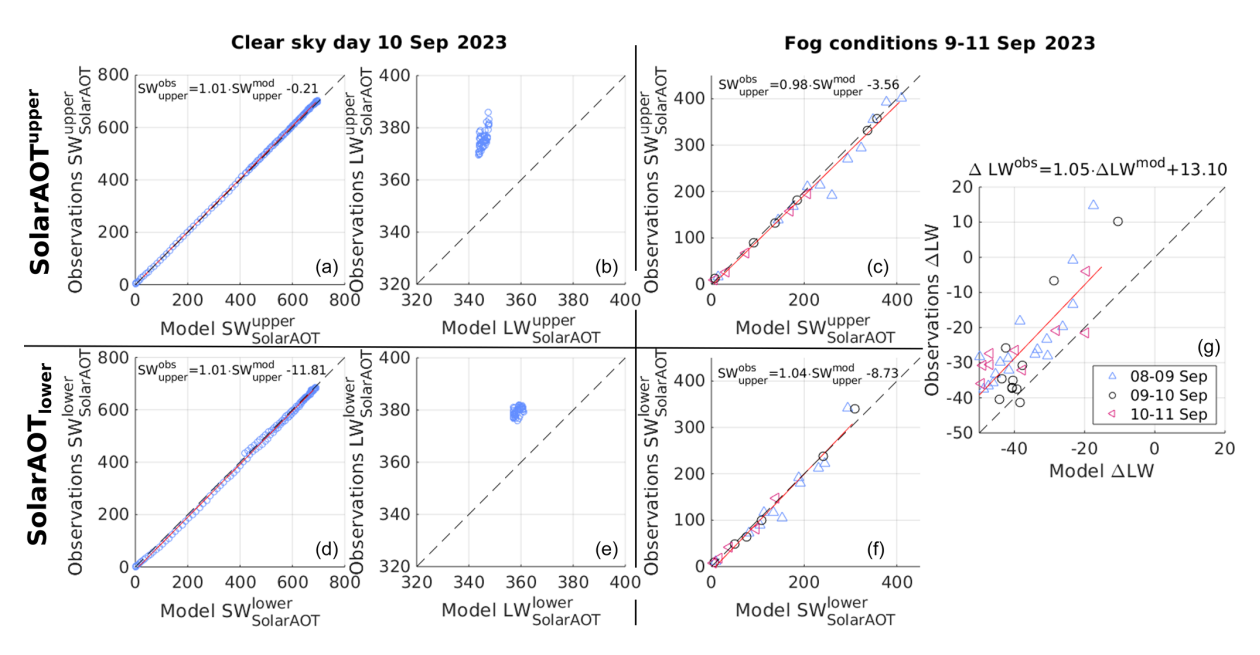


Figure 12. Scatter plots comparing observed and modeled SW (a, d, c, f) and LW (b, e, g) fluxes under clear-sky (a, b, d, e) and fog conditions (c, f, g). The last column presents the difference (Δ) between upper and lower station measurements for observed and modeled LW flux in fog conditions. The red solid line indicates the linear fit to the data. Blue triangles represent measurements from the night of 8–9 September, black circles show fog data from the night of 9–10 September, and pink triangles correspond to data collected during the night of 10–11 September 2023. The equation for each fit is shown in the corresponding panel.

Table 2. Statistics of SW (I) and LW (IR) flux comparisons between the model and observations at both sites. The mean bias error (MBE) and root mean square error (RMSE) were calculated for each day under fog and non-fog conditions. Additionally, for 9 September, the mean MBE and RMSE for the SW radiation were computed after removing the estimated cirrus-induced bias.

MBE $[W m^{-2}]$									
Night between	8–9	Sep	9–10) Sep	10–11 Sep				
Model run	every 5 min	when sounding	every 5 min	when sounding	every 5 min	when sounding			
Fog implementation	no	yes	no	yes	no	yes			
Time	07:00-17:00 UTC	04:00-07:00 UTC	07:00-17:00 UTC	04:00-07:00 UTC	07:00-17:00 UTC	4 −07:00 UTC			
I _{SolarAOT} upper	-12.9 ± 22.3	12.7 ± 23.1	-4.5 ± 2.9	1.4 ± 3.3	_	6.5 ± 5.8			
I _{SolarAOT_{lower}}	-1.0 ± 23.1	8.2 ± 23.7	6.7 ± 8.1	-1.5 ± 15.4	_	-0.3 ± 8.9			
I _{SolarAOT_{lower}} (-cirrus bias)	11.9 ± 13.9	0.8 ± 26.0							
Time	10:00-14:00 UTC	00:00-07:00 UTC	10:00-14:00 UTC	0 - 07:00 UTC		00:00-07:00 UTC			
IR _{SolarAOT} upper	-29.9 ± 2.9	-3.7 ± 3.8	-32.4 ± 2.3	2.6 ± 3.4	_	0.3 ± 6.0			
IR _{SolarAOT_{lower}}	-20.7 ± 1.5	9.3 ± 8.6	-22.3 ± 3.1	10.8 ± 7.9	_	12.2 ± 3.3			
RMSE [W m ⁻²]									
Night between	8–9 Sej	ptember	9–10 Se	ptember	10–11 September				
Model run	every 5 min	when sounding	every 5 min	when sounding	every 5 min	when sounding			
Fog implementation	no	yes	no	yes	no	yes			
Time	07:00-17:00 UTC	04:00-07:00 UTC	07:00-17:00 UTC	04:00-07:00 UTC	07:00-17:00 UTC	04:00-07:00 UTC			
I _{SolarAOT} upper	25.7	25.4	5.4	3.3	_	8.4			
I _{SolarAOT_{lower}}	23.1	24.0	10.5	14.1	_	8.0			
I _{SolarAOT_{lower}} (-cirrus bias)	18.2	24.8							
Time	10:00-14:00 UTC	00:00-07:00 UTC	10:00-14:00 UTC	00:00-07:00 UTC		00:00-07:00 UTC			
IR _{SolarAOT} upper	30.1	5.3	32.5	4.1	_	5.7			
IR _{SolarAOT_{lower}}	20.8	12.5	22.5	13.2	_	12.6			

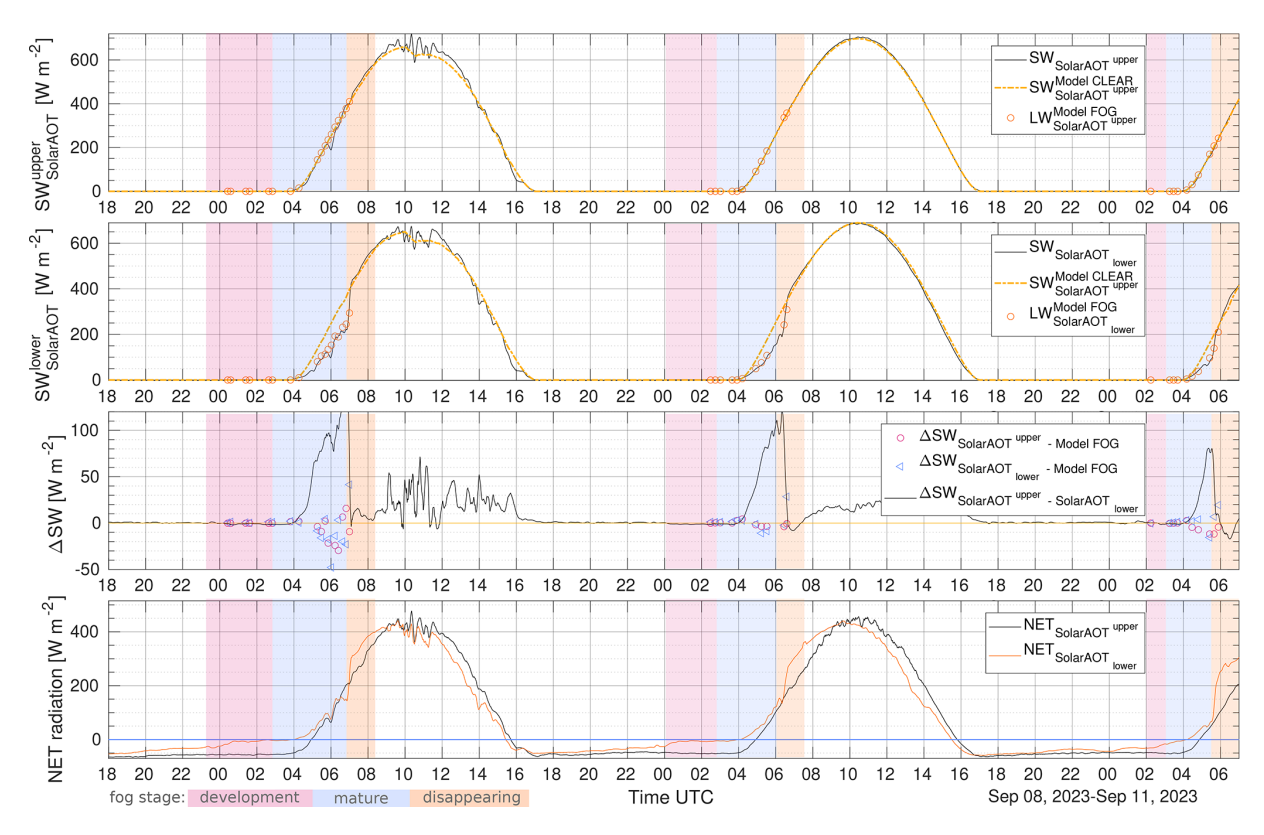


Figure 13. Incoming SW flux for SolarAOT^{upper} and SolarAOT_{lower} station. The black solid line measured data, the yellow dashed line model results for no fog conditions, and the orange circles model results for fog conditions measured by soundings. The third panel from the top presents the difference in SW flux between the upper and lower site (solid line), and pink circles represent the difference between SolarAOT^{upper} station and model when fog conditions were implemented. Blue triangles represent the difference between the SolarAOT_{lower} station and the model with implemented fog conditions. The lowest panel presents the total net radiation for SolarAOT^{upper} (black line) and SolarAOT_{lower} station (orange line).

upper station it was $-49 \, \mathrm{W \, m^{-2}}$. Starting at 02:00, the net radiation gradually increased from approximately $-30 \, \mathrm{m^{-2}}$ and reached $0 \, \mathrm{m^{-2}}$ at sunrise. The fog disappeared quickly, in less than $10 \, \mathrm{min}$; at 05:35 the NET radiation changed by $125 \, \mathrm{W \, m^{-2}}$.

Having information on radiation fluxes at two levels allows for investigating the sensitivity of the change in LW radiation by the fog LWP. Figure 15 shows the relationship between the modeled LWP content and the modeled difference in LW radiation between the upper and lower stations. In addition to the modeled values, the lower panel of Fig. 15 shows the relationship for the data observed at both stations and the measured LWP on the balloon in the fog. In both graphs, the data exhibit a linear relationship, with Pearson correlation coefficients and corresponding p values of -0.82 and 1.79×10^{-10} for the model and -0.37 and 0.02 for the observations, respectively. A straight line was fitted to the modeled data, given by the following equation:

$$\Delta IR = -1.09 [Wg^{-1}] \cdot LWP - 13.42 [Wm^{-2}]. \tag{17}$$

A straight line was fitted to the observed data:

$$\Delta IR = -0.74 [Wg^{-1}] \cdot LWP + 12.25 [Wm^{-2}]. \tag{18}$$

5 Conclusions

The purpose of this study was to capture vertical profiles of the microphysical and thermodynamic characteristics within fog layers, using in situ data collected by a tethered balloon during a field campaign. This article analyzes three cases of radiative fog that occurred in the valley of the city of Strzyżów (Southeastern Poland) in September 2023. In total, 74 soundings were performed, 41 of which included measurements with the OPC-N3 sensor, enabling the calculation of droplet size spectra. The three observed cases exhibited similar meteorological conditions, including temperature (T), relative humidity (RH), and aerosol scattering coefficient at 525 nm (ASC₅₂₅). For each case, the liquid water path (LWP) exceeded 15 g m⁻², and in most instances, the fog did not transition into thick fog.

In quasi-adiabatic stratiform clouds, increases in liquid water content (LWC) are typically associated with droplet growth, with number concentrations (N_c) remaining relatively constant (Brenguier et al., 2000; Chang and Li, 2002).

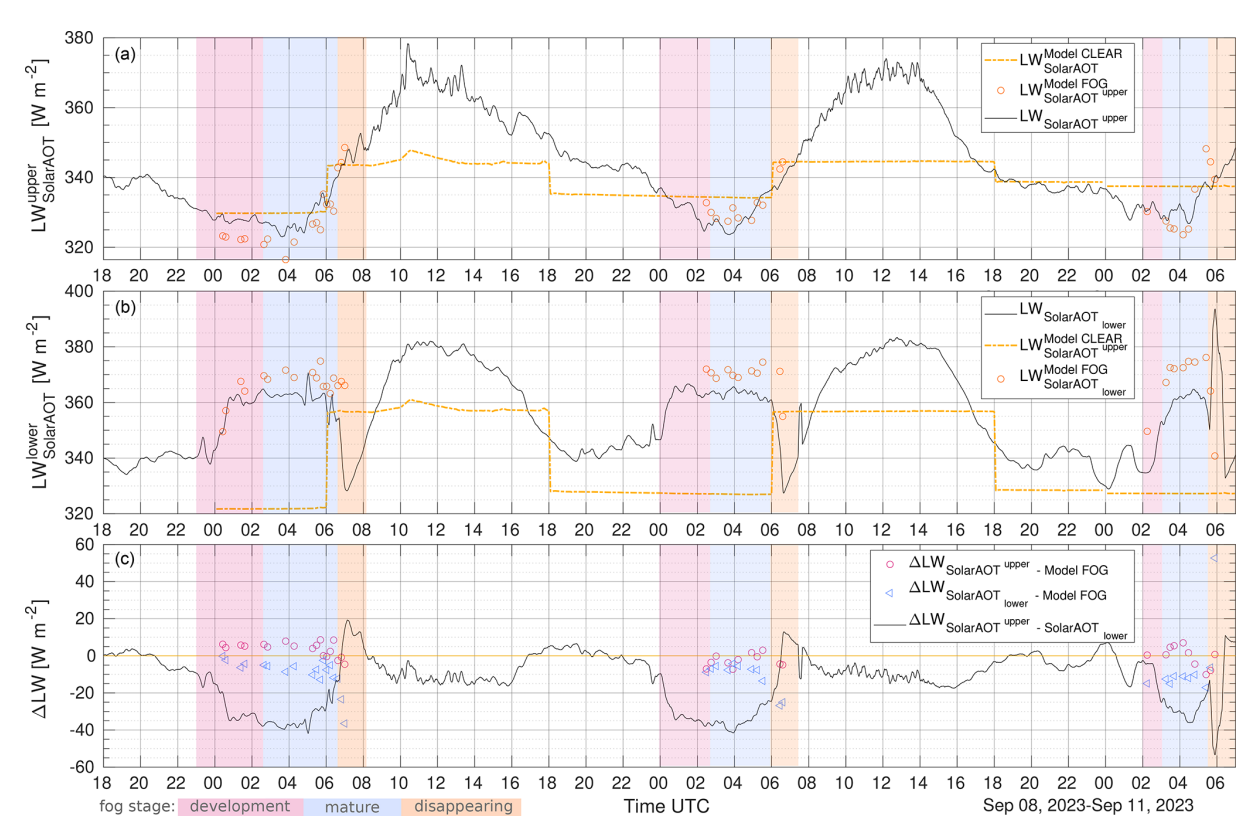


Figure 14. Incoming LW flux for SolarAOT^{upper} (a) and SolarAOT_{lower} station (b). The black solid line measured data, the yellow dashed line model result for no fog conditions, and the orange circles model results for fog conditions measured by soundings. Panel (c) presents the difference in LW flux between SolarAOT^{upper} and SolarAOT_{lower} station with the solid line, pink circles represent the difference between the upper station and the model with fog conditions implemented, and blue triangles represent the difference between lower station and model with fog conditions.

In contrast, our fog observations showed that LWC increases were primarily driven by increases in $N_{\rm c}$, indicating droplet activation rather than growth via coalescence. This agrees with findings from earlier fog studies (Okita, 1962; Egli et al., 2015). The vertical structure of fog microphysics showed consistent patterns across all three cases. The effective radius ($r_{\rm eff}$) decreases with height, as fog matured; this decrease became less pronounced. This is consistent with Okita (1962) and partially with the observations of Egli et al. (2015) (in his study, $r_{\rm eff}$ decreased with height in some cases but was mostly constant with height).

The droplet size distribution (DSD) revealed two dominant regimes: small droplets (4–5 μ m) that increased in importance with height and fewer but water-rich large droplets (> 18.5 μ m) of which significance decreased with height. These large droplets, though rare, contributed significantly to the total water content. Similarly in the work of Okita (1962), large droplets are mostly concentrated near the ground. Fog DSDs with small concentrations of drops greater than 30 μ m were also observed in experiments conducted by Wendish et al. (1998), Gultepe et al. (2009), and Mazoyer et al. (2022). These large droplets are the result of collision—coalescence

and Ostwald ripening processes. This bimodal structure is especially relevant for modeling, as current numerical weather prediction (NWP) and large eddy simulation (LES) frameworks typically use bulk microphysical schemes that assume a single-mode droplet population. These schemes are based on simplified parameters such as LWP and N_c (Bergot et al., 2007; Khain et al., 2015) and do not resolve the vertical variability or the coexistence of distinct droplet regimes. As a result, larger droplets - which play a key role in sedimentation and fog dissipation – are not properly represented, potentially leading to persistent overestimation of LWC in fog forecasts (Philip et al., 2016; Pithani et al., 2019). Incorporating full droplet spectra across the fog layer, including both small and large droplets, would allow models to more accurately simulate fog formation and dissipation (Thoma et al., 2011).

To support future fog modeling efforts, we applied the concept of equivalent adiabaticity (α_{eq}) across different fog stages, a relatively new parameter proposed in recent literature. The computed α_{eq} values ranged from 0.0 to 0.6, consistent with previous studies of fog. During one case, at the early stage of fog development, a negative value of α_{eq} was

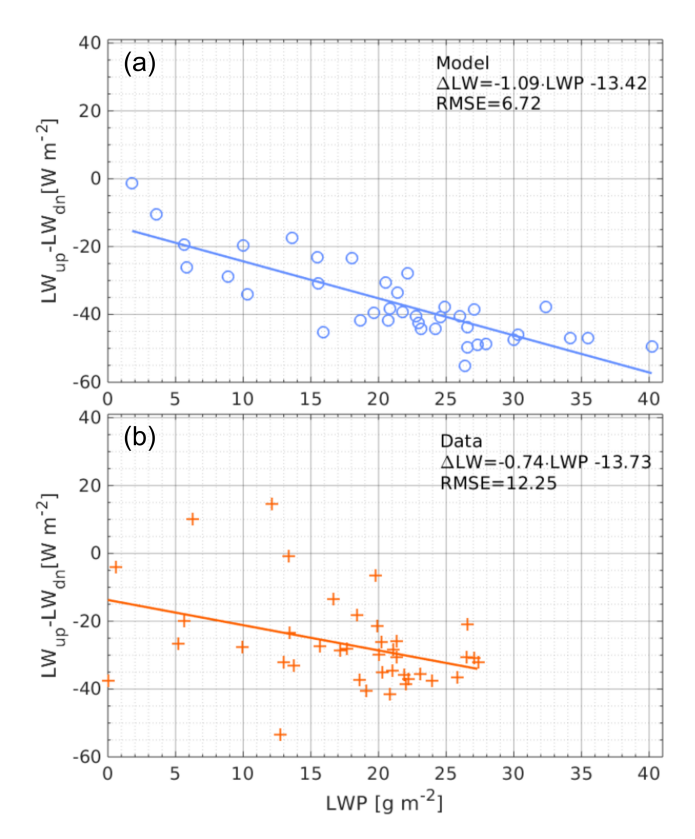


Figure 15. Relation between fog LWP (for days 9–11 September 2023) and the difference of LW downward flux between the upper and lower SolarAOT stations. The upper panel presents the radiation transfer model simulations, and the lower panel corresponds to the balloon profiles (LWP) and radiometer observations at the upper and lower SolarAOT stations.

observed (-3.2). This negative value was attributed to an elevated LWC near the ground. In the literature, cases where LWC decreases with height in fog are rarely observed and are typically associated with thin fog layers, with CTH not exceeding 40 m (Costabloz et al., 2025; Okita, 1962; Boutle et al., 2018).

We quantified mean microphysical values for optically thin fogs in valley conditions. The fog-core LWC ranged from 0.2 to $0.4 \,\mathrm{g}\,\mathrm{m}^{-3}$, and $N_{\rm c}$ reached up to $300\,\mathrm{cm}^{-3}$. The mean $r_{\rm eff}$ in all cases was around $8{\text -}10\,\mathrm{\mu}\mathrm{m}$ and decreased linearly with height. While the vertical profile of LWC could be approximated by a linear function, increasing from the ground up to approximately $60\,\%$ of the fog top height (CTH) and then decreasing toward the top, the mean $N_{\rm c}$ profile followed a parabolic shape during the nights of $8{\text -}9$ and $9{\text -}10$ September. In the final case (10–11 September), $N_{\rm c}$ exhibited two local maxima, located at approximately $25\,\%$ and $88\,\%$ of CTH.

In contrast to the commonly held assumption that fog dissipates primarily from the top, our observations show that in all three analyzed cases – characteristic of optically thin fog – dissipation occurred simultaneously from both the top

and bottom. The dissipation process is difficult to capture, as it typically occurs within a short time frame of $15-30\,\mathrm{min}$. During the dissipation stage, the region above the maximum N_c/LWC becomes compressed, likely due to solar heating from above. The maximum of N_c/LWC shifts upward to above 80% of the fog height. We propose that the bottom dissipation is linked to surface warming caused by shortwave radiation penetrating the optically thin fog layer. As the ground heats up, the relative humidity near the surface decreases, leading to the evaporation of the smallest droplets. As no new droplets are formed, the remaining larger droplets settle and accumulate near the ground, which is reflected in increased $r_{\rm eff}$ values at the base of the fog.

Droplets with radii up to $40 \,\mu\text{m}$ can be described by an approximate formula for terminal velocity (u):

$$u(r) = k_1 \cdot r^2,\tag{19}$$

where $k_1 \approx 1.19 \times 10^6 \, \mathrm{cm^{-1} \, s^{-1}}$ (Yau and Rogers, 1996). Using this formula, the fall velocity for droplets larger than 18.5 µm is approximately $4.07 \, \mathrm{cm \, s^{-1}}$. In the absence of droplet growth and turbulence, such droplets will be removed from a 100 m thick fog layer within about 7 min. During soundings conducted at the final stage of the fog life cycle, no large droplets were observed, indicating that they had already settled out.

Finally, we assessed the radiative impacts of fog using dual-level radiometers. At the Strzyżów location, solar and infrared radiometers are installed at two different heights (within the fog layer and above it). A linear relationship was found between infrared radiation reduction and fog water content (Pearson correlation coefficients and corresponding p values of -0.82 and 1.79×10^{-10} for the model and -0.37 and 0.02 for the observations, respectively). The dissipation of fog caused rapid changes (within 10–30 min) in surface radiation fluxes of up to 160 W m^{-2} . During fog, the mean bias between observed and modeled radiation fluxes is approximately 2 W m^{-2} for shortwave (SW) and 11 W m^{-2} for longwave (LW) radiation at the lower station, supporting the reliability of the retrieved microphysical inputs.

In summary, this study provides detailed observational evidence of fog microphysics and dynamics under valley conditions. These findings not only refine our understanding of fog development and dissipation but also offer actionable data for improving fog representation in weather models.

Appendix A: Temperature setup in the model

The *T* and RH data were taken from HYT and GY-63 and interpolated to the levels of the model. As the measurements mostly reached 115 m, above, the temperature and humidity profile was set according to the measurement from atmospheric sounding from Tarnów (WMO station 12575) done by IMGW (Polish Institute of Meteorology and Water Management). Tarnów is 60 km in a straight line from the city

of Strzyżów. For a better description of the merging of data, sounding from Tarnów will be called sounding T.

To have a smooth transition between balloon sounding and the soundingT, the data from the balloon and soundingT were stitched together. For this purpose, first, the points were extrapolated so that at the stitching point, the values from both soundings were available. The procedure was performed for the last three points (highest points) from the balloon profile and the first two points of soundingT above the balloon profile. Then, for these five points, the average value weighted by the distance of the points was taken. As the soundingT does not always reach 10 km, above soundingT the standard atmosphere profile for mid-latitude summer was used.

As the profile of RH was stitched and interpolated, the precipitable water (PW) was changed. To fix this issue, the whole profile of RH was rescaled in such a way that PW is the same as the PW obtained from sounding T before interpolating.

Appendix B: Additional tables and figures

Table B1. List of abbreviations.

Abbreviation	Description	Abbreviation	Description
AE	aerosol Ångström exponent	MSE	mean bias error
$\alpha_{ m eq}$	theoretical equivalent adiabaticity	MWR	microwave radiometer
AOD	aerosol optical depth	NTSB	American National Transportation Safety Board
ASC ₅₂₅	aerosol scattering coefficient of light at 525 nm	LES	large eddy simulation
CCN	cloud condensation nuclei	LW	longwave radiation
CTH	cloud/fog top height	LWC	liquid water content
DSD	droplet size distribution	LWC ₀	non-zero surface liquid water content
eBC	equivalent of black carbon	LWP	liquid water path
$N_{\rm c}$	droplet number concentration	RH	relative humidity
NC	particle number concentration	RMSE	root mean square error
NWP	numerical weather prediction	SBL	stable boundary layer
p	pressure	SSA	aerosol single scattering albedo
PM	particle matter	SW	shortwave radiation
$r_{ m eff}$	effective radius	T	temperature
RH	relative humidity	vDSD	volume droplet size distribution

Table B2. Apparatus used during each of the soundings of case study 9–11 September 2023. Markers represent: ▶ setup with OPC-N3, ◆ setup with radiosonde, ▲ setup with OPC-N3 and radiosonde, and \Box problems with collected data (soundings with partially recorded data were not taken into further analysis.

Sounding no.	Day	Time	Radiosonde	AE-51	GY63	HYT	OPC-N3	SPS30	Sounding no.	Day	Time	Radiosonde	AE-51	GY63	HYT	OPC-N3	SPS30	Sounding no.	Day	Time	Radiosonde	AE-51	GY63	HYT	OPC-N3	SPS30
1	08	20:29-20:42							28	09	17:59–18:10	•	•					54	11	02:11-02:17			•	•	•	•
2	08	21:00-21:35							29	10	00:41-00:51							55	11	02:19-02:26						
3	08	22:24-22:34							30	10	00:53-01:05	•						56	11	02:29-02:37						
4	09	00:22-00:28			•	•	•	•	31	10	01:18-01:28							57	11	02:43-03:02	•					
5	09	00:30-00:40			•	•	•	•	32	10	01:37-01:46							58	11	03:10-03:20			•	•	•	•
6	09	00:48-01:01	•						33	10	01:55-02:04	•						59	11	03:23-03:33			•	•	•	•
7	09	01:20-01:27			•	•	•	•	34	10	02:24-02:34			•	•	•	•	60	11	03:36-03:46			•	•	•	•
8	09	01:32-01:41			•	•	•	•	35	10	02:40-02:48			•	•	•	•	61	11	03:49-03:59	•					
9	09	02:34-02:42			•	>	•	•	36	10	02:54-03:06			•	•	•	•	62	11	04:04-04:16			•	•	•	•
10	09	02:45-02:55			•	•	•	•	37	10	03:09-03:23	•						63	11	04:19- 04:36			•	•	•	•
11	09	03:03-03:27	•						38	10	03:33-03:44			•	•	>	•	64	11	04:40-04:56			•	•	•	•
12	09	03:34-04:03			•	>	•	•	39	10	03:49-04:00			•	•	•	•	65	11	04:59-05:15	•					
13	09	04:09-04:22			•	•	•	•	40	10	04:06-04:17			•	•	•	•	66	11	05:19-05:30			•	•	•	•
14	09	05:10-05:21			•	•	•	•	41	10	04:20-04:40	•						67	11	05:32-05:45			•	•	>	•
15	09	05:23-05:34			•	•	•	•	42	10	04:50-05:00			•	•	•	•	68	11	05:47-05:59			•	•	•	•
16	09	05:37-05:45			•	•	•	>	43	10	05:06-05:21			•	•	>	>	69	11	06:02-06:11	•	•				
17	09	05:47-05:54	•		•	•	•	•	44	10	05:25-05:37			•	•	•	•	70	11	06:18-06:33	•	•				
18	09	05:56-06:06	A		•	A	A	A	45	10	05:40-05:56	•						71	11	06:39-06:53			•	•	•	•
19	09	06:09-06:17	A		A	A	A	A	46	10	06:03-06:13							72	11	06:56-07:14	•	•				
20	09	06:19-06:28	A		A	A	A	A	47	10	06:23-06:31			•	•	>	•	73	11	07:15-07:29	•	•				
21	09	06:33-06:42	A		A	A	A	A	48	10	06:31-06:40			•	•	•	•	74	11	07:36-07:51	•	•				
22	09	06:45-06:53	A		A	A	A	A	49	10	06:42-06:50	•	•													
23	09	06:56-07:03	A		A	A	A	A	50	10	06:52-07:00															
24	09	07:07-07:13	A		A	A	A	A	51	10	07:01-07:19	•	•													
25	09	07:18-07:41	•	•					52	10	07:11-07:17															
26	09	07:42-07:56	•	•					53	10	07:22-07:32	•	•													
27	09	07:57-08:08	•	•																						

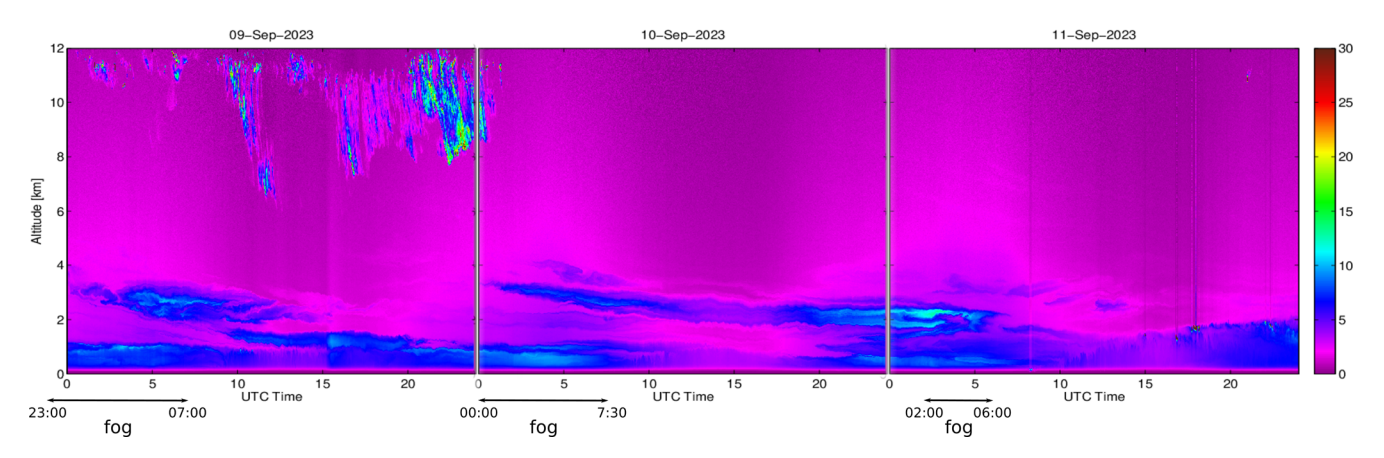


Figure B1. Temporal variability of 510 M lidar-range-corrected signal (at 532 nm) from the level of the upper station up to 12 km between 9 and 11 September 2023.



Figure B2. Visualization of radiation fog top. Photos were taken with the camera at the SolarAOT^{upper} station at 04:00 UTC each day.

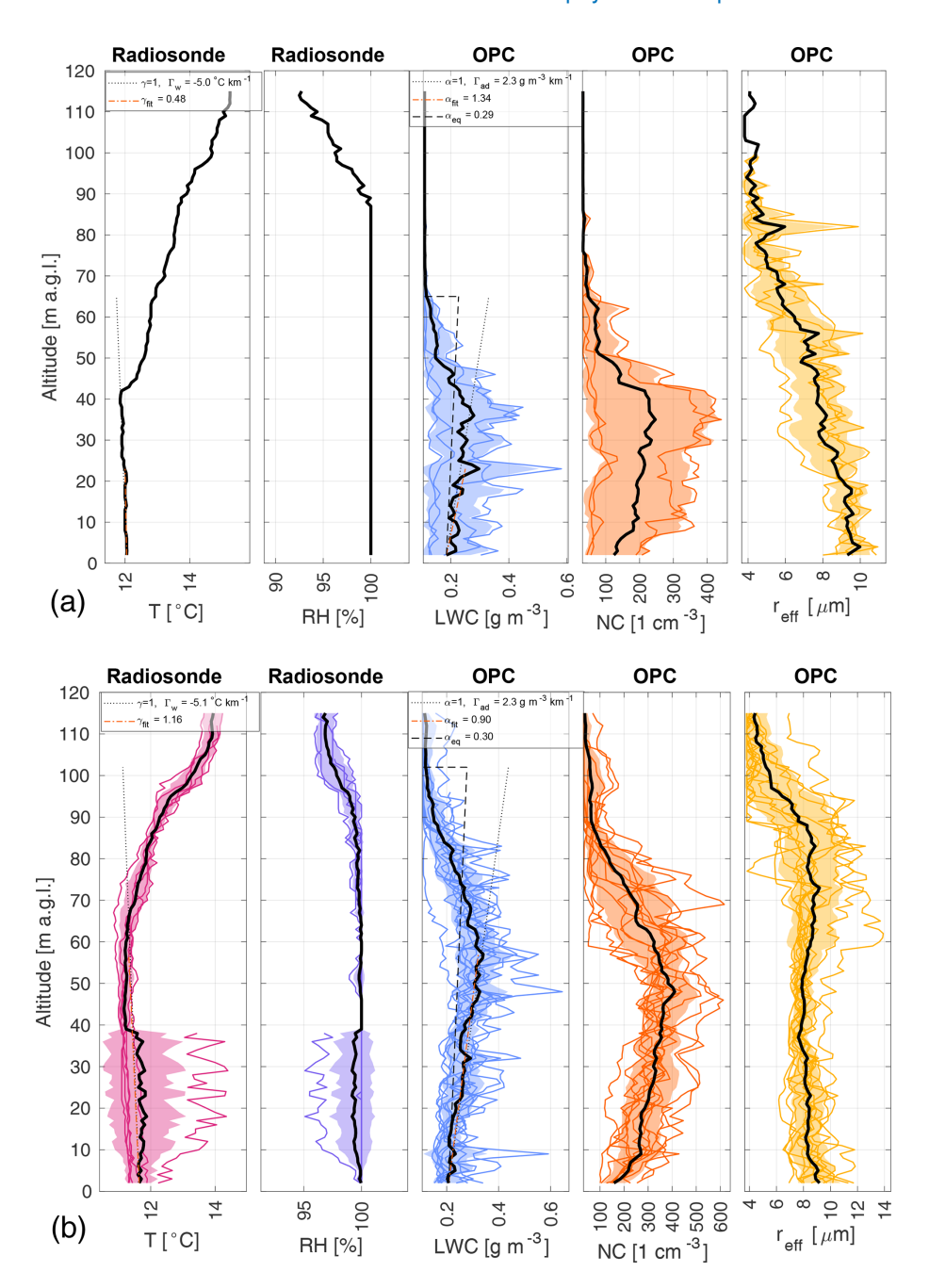


Figure B3. Panels present specific quantities measured by the balloon for each stage of fog observed during the night of 8–9 September 2023. (a) Development stage of fog. (b) Mature state of fog. Detailed description in the caption of Fig. B4.

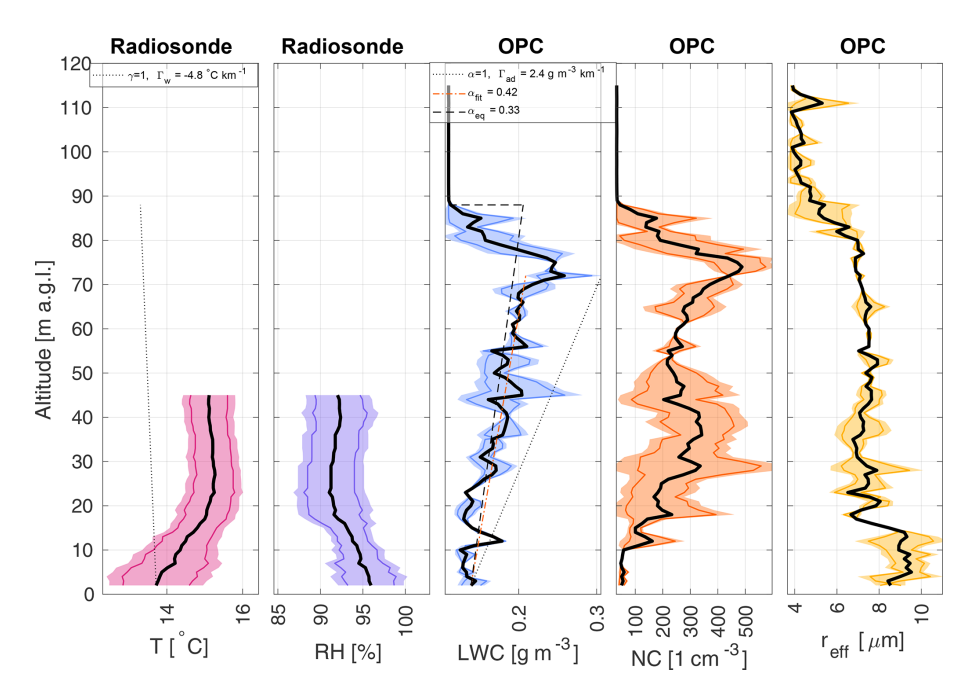


Figure B4. Disappearing stage of fog. Panels present specific quantities measured by the balloon for each stage of fog observed during the night of 8–9 September 2023. From left: T from Vaisala radiosonde RS41, RH from Vaisala radiosonde RS41, N_c , and r_{eff} within the fog. Each colored line represents one balloon profile. The black thick line represents the mean of all the soundings, and the colored area represents the range between \pm standard deviation from the mean. In the T plot, the dotted line presents the lapse rate, and the dashed red line presents the linear fit to T from 2 m to the height of maximum mean LWC. In the LWC plot, the dotted line presents the LWC adiabatic lapse rate, and the dashed red line presents the linear fit to LWC from 2 m to the height of maximum mean LWC.

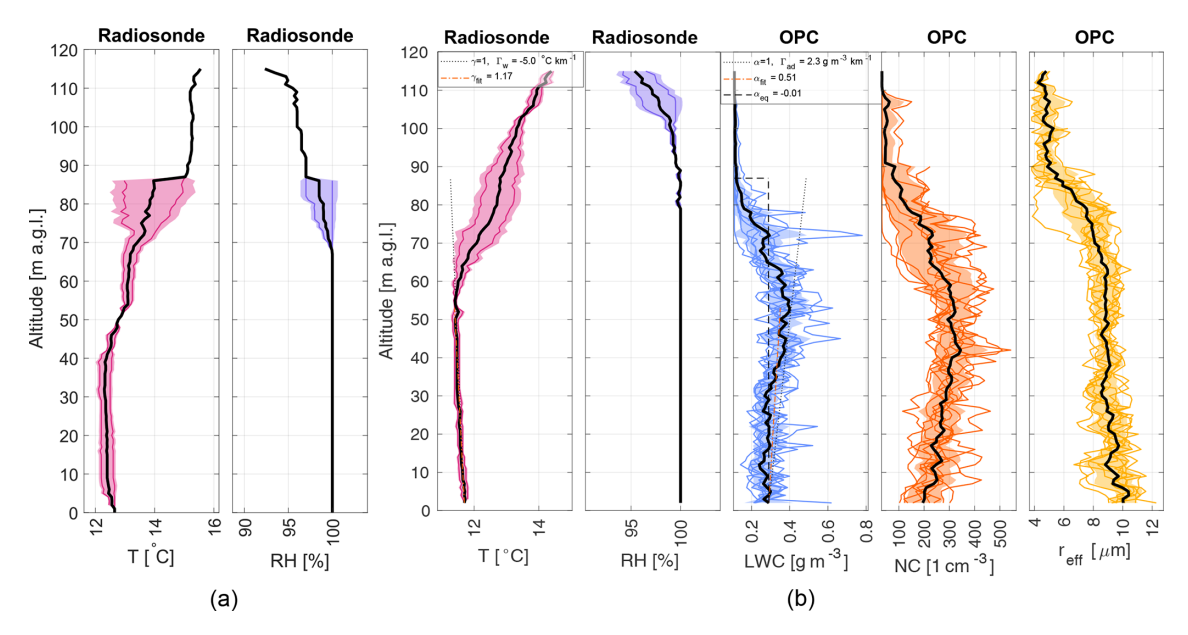


Figure B5. Panels present specific quantities measured by the balloon for each stage of fog observed during the night of 10–11 September 2023. (a) Development stage of fog. (b) Mature state of fog. Detailed description in the caption of Fig. B6.

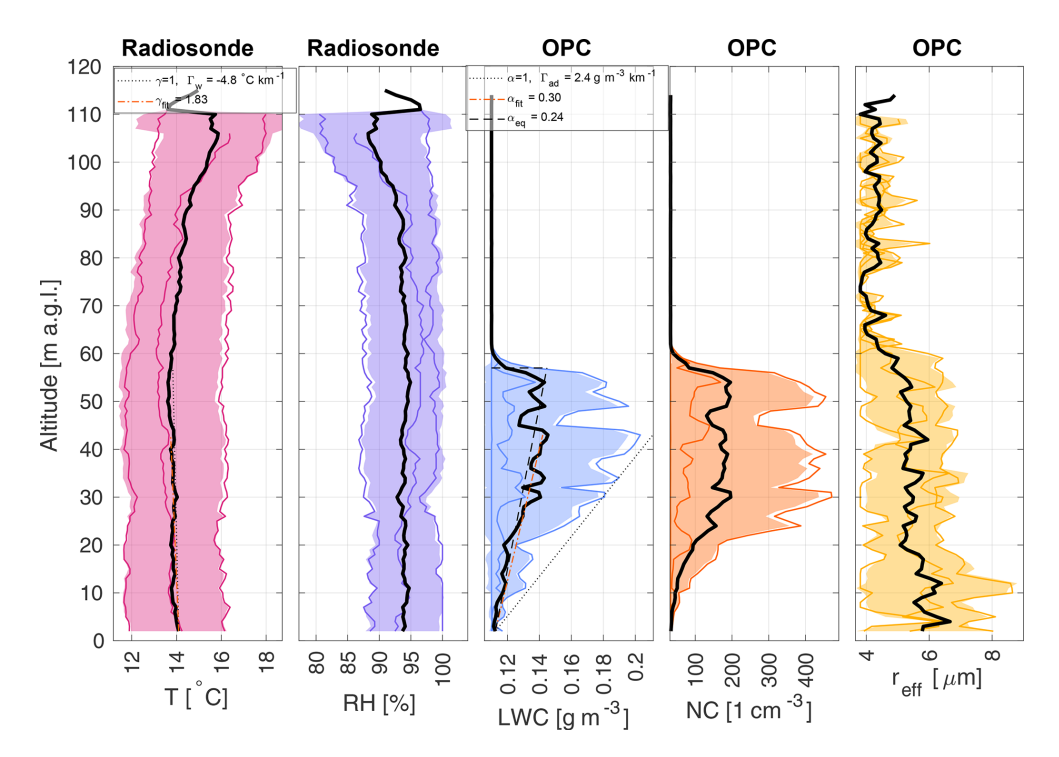


Figure B6. Disappearing stage of fog. Panels present specific quantities measured by the balloon for each stage of fog observed during night of 9–10 September 2023. From left: T from Vaisala radiosonde RS41, RH from Vaisala radiosonde RS41, N_c , and r_{eff} within the fog. Each colored line represents one balloon profile. The black thick line represents the mean of all the soundings, and the colored area represents the range between \pm standard deviation from the mean. In the T plot, the dotted line presents the lapse rate, and the dashed red line presents the linear fit to T from 2 m to the height of maximum mean LWC. In the LWC plot, the dotted line presents the LWC adiabatic lapse rate, and the dashed red line presents the linear fit to LWC from 2 m to the height of maximum mean LWC.

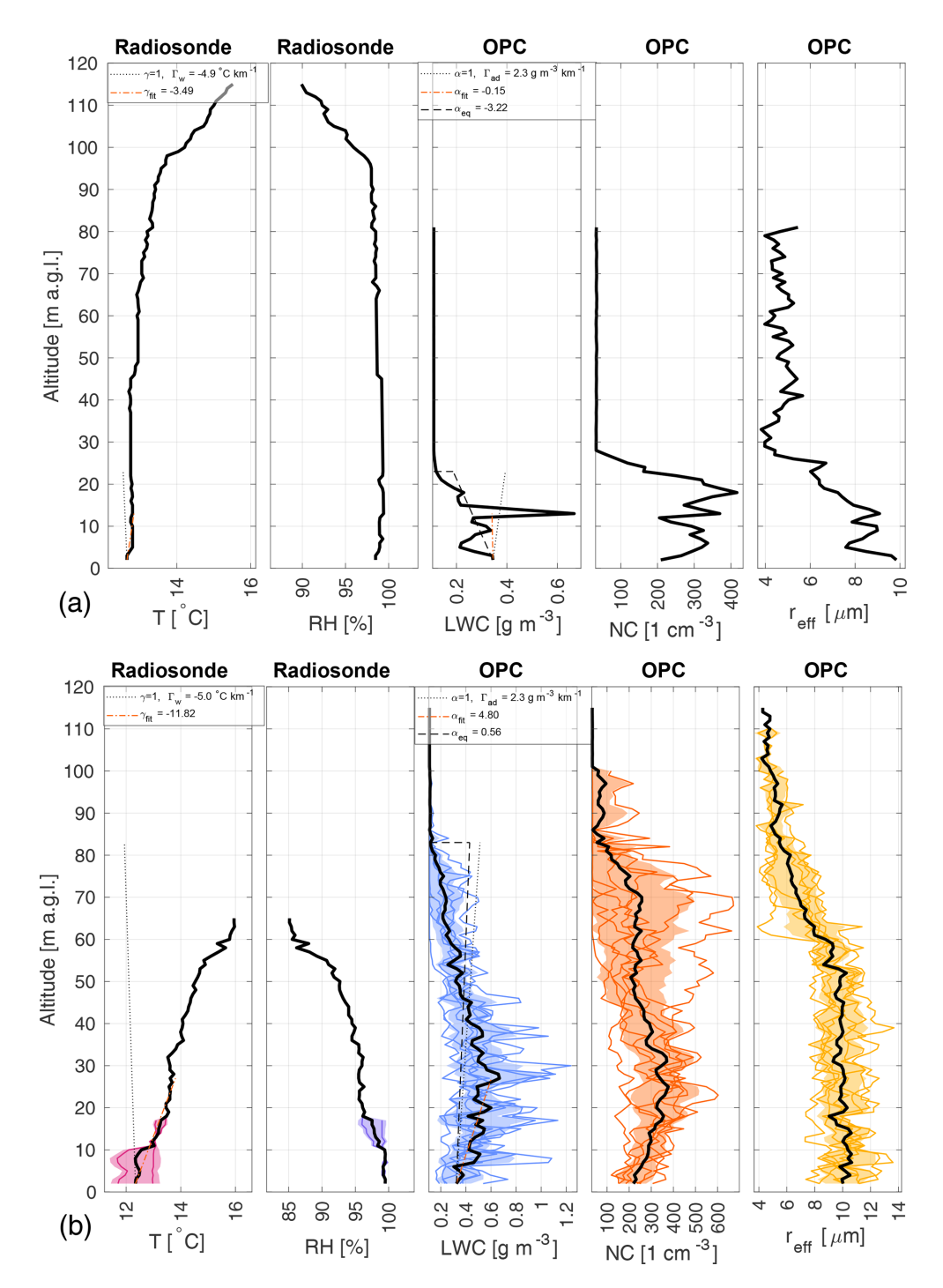


Figure B7. Panels present specific quantities measured by the balloon for each stage of fog observed during the night of 10–11 September 2023. (a) Development stage of fog. (b) Mature state of fog. Detailed description in the caption of Fig. B8.

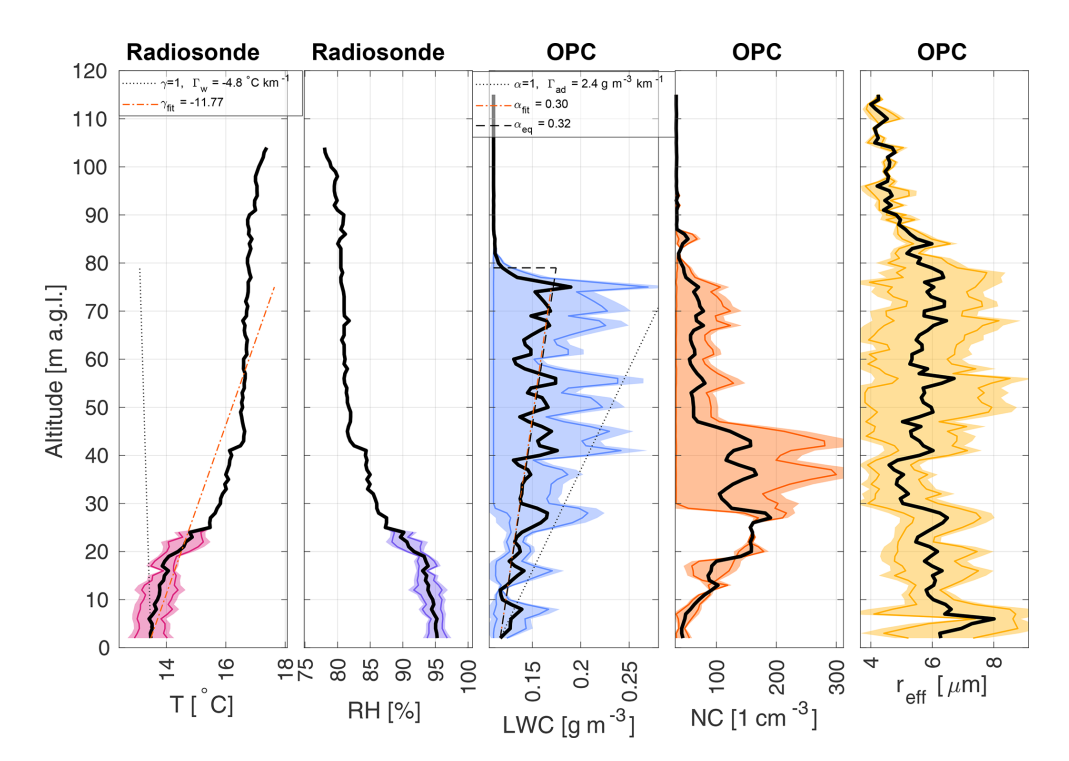


Figure B8. Disappearing stage of fog. Panels present specific quantities measured by the balloon for each stage of fog observed during the night of 10-11 September 2023. From left: T from Vaisala radiosonde RS41, RH from Vaisala radiosonde RS41, N_c , and r_{eff} within the fog. Each colored line represents one balloon profile. The black thick line represents the mean of all the soundings, and the colored area represents the range between \pm standard deviation from the mean. In the T plot, the dotted line presents the lapse rate, and the dashed red line presents the linear fit to T from 2 m to the height of maximum mean LWC. In the LWC plot, the dotted line presents the LWC adiabatic lapse rate, and the dashed red line presents the linear fit to LWC from 2 m to the height of maximum mean LWC.

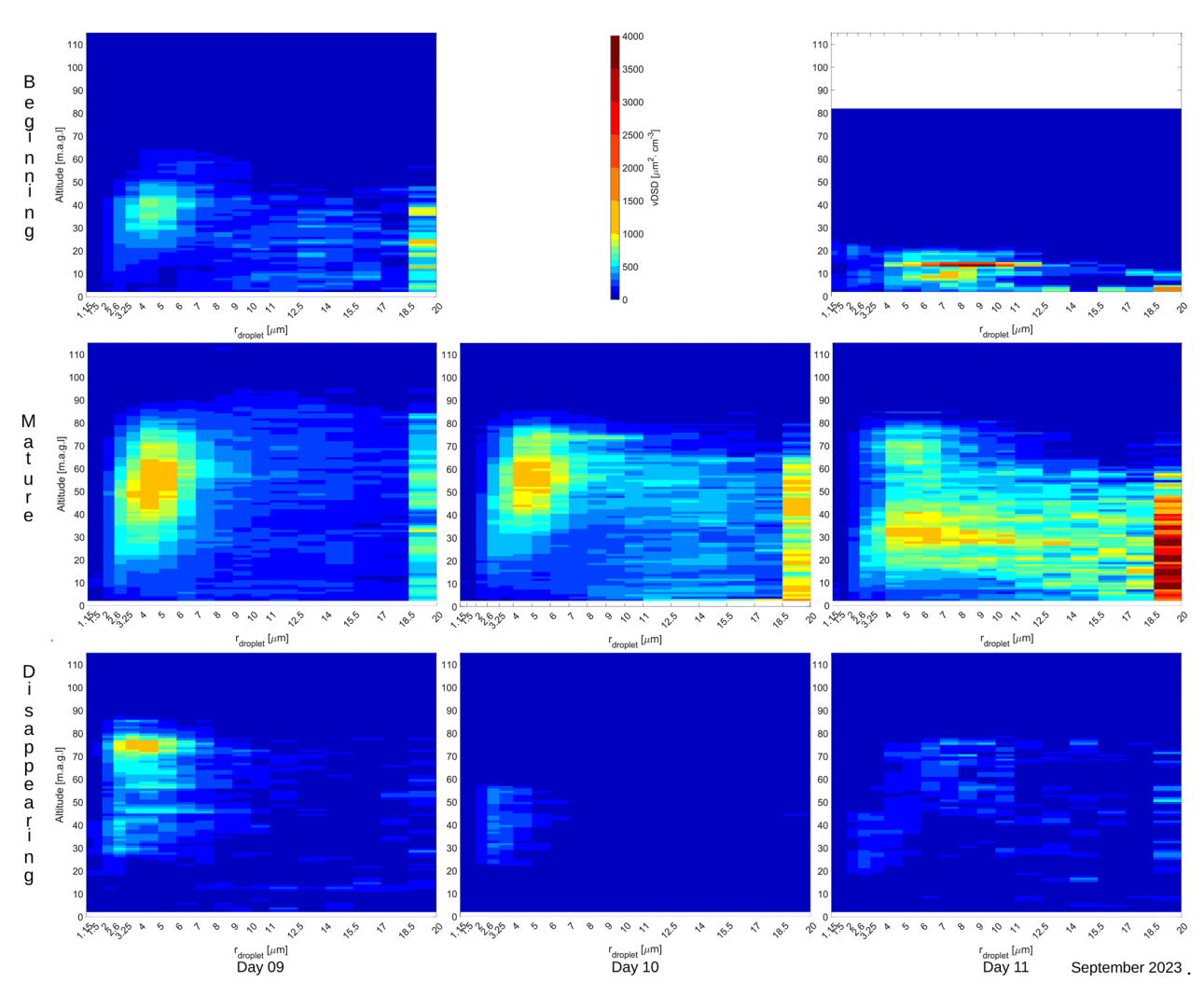


Figure B9. Profiles with height of vDSD for 9–11 September 2023 fog occurrence. Different days are in columns, in rows from the top: beginning, mature, and disappearing stage of fog.

Data availability. The data used in this article were uploaded to the following repository: https://doi.org/10.58132/WPKQNT (Nurowska, 2025).

Author contributions. KN – conceptualization, methodology, formal analysis, investigation, writing (original draft preparation and review and editing), visualization; PM – lidar data visualization; KM – conceptualization, supervision. All authors have read and agreed to the published version of the manuscript.

Competing interests. The contact author has declared that none of the authors has any competing interests.

Disclaimer. Publisher's note: Copernicus Publications remains neutral with regard to jurisdictional claims made in the text, published maps, institutional affiliations, or any other geographical representation in this paper. While Copernicus Publications makes every effort to include appropriate place names, the final responsibility lies with the authors. Views expressed in the text are those of the authors and do not necessarily reflect the views of the publisher.

Acknowledgements. We thank the AERONET team, principal investigators, and other participants for their effort in establishing and maintaining the network. This research is part of the OPUS project (Polish grant no. 2017/27/B/ST10/00549) "Impact of aerosol on the microphysical, optical and radiation properties of fog", which was funded by the National Science Centre, coordinated by the Institute of Geophysics, Faculty of Physics, University of Warsaw.

Financial support. This research has been supported by the National Science Centre (grant no. 2017/27/B/ST10/00549).

Review statement. This paper was edited by Michael Tjernström and reviewed by Graham Weedon and one anonymous referee.

References

- Antoine, S., Honnert, R., Seity, Y., Vié, B., Burnet, F., and Martinet, P.: Evaluation of an Improved AROME Configuration for Fog Forecasts during the SOFOG3D Campaign, Weather and Forecasting, 38, 1605–1620, https://doi.org/10.1175/WAF-D-22-0215.1, 2023.
- Bari, D., Bergot, T., and Tardif, R.: Fog Decision Support Systems: A Review of the Current Perspectives, Atmosphere, 14, https://doi.org/10.3390/atmos14081314, 2023.
- Bergot, T., Terradellas, E., Cuxart, J., Mira, A., Leichti, O., Mueller, M., and Nielsen, N. W.: Intercomparison of singlecolumn numerical models for the prediction of radiation fog, Journal of Applied Meteorology and Climatology, 46, 504–521, https://doi.org/10.1175/JAM2475.1, 2007.
- Bergot, T., Escobar, J., and Masson, V.: Effect of small-scale surface heterogeneities and buildings on radiation fog: Large-eddy simulation study at Paris–Charles de Gaulle airport, Quarterly Journal of the Royal Meteorological Society, 141, 285–298, https://doi.org/10.1002/qj.2358, 2015.
- Betts, A. K.: Cloud Thermodynamic Models in Saturation Point Coordinates, Journal of Atmospheric Sciences, 39, 2182–2191, https://doi.org/10.1175/1520-0469(1982)039<2182:CTMISP>2.0.CO;2, 1982.
- Boutle, I., Price, J., Kudzotsa, I., Kokkola, H., and Romakkaniemi, S.: Aerosol–fog interaction and the transition to well-mixed radiation fog, Atmos. Chem. Phys., 18, 7827–7840, https://doi.org/10.5194/acp-18-7827-2018, 2018.
- Boutle, I., Angevine, W., Bao, J.-W., Bergot, T., Bhattacharya, R., Bott, A., Ducongé, L., Forbes, R., Goecke, T., Grell, E., Hill, A., Igel, A. L., Kudzotsa, I., Lac, C., Maronga, B., Romakkaniemi, S., Schmidli, J., Schwenkel, J., Steeneveld, G.-J., and Vié, B.: Demistify: a large-eddy simulation (LES) and single-column model (SCM) intercomparison of radiation fog, Atmos. Chem. Phys., 22, 319–333, https://doi.org/10.5194/acp-22-319-2022, 2022.
- Brenguier, J. L.: Parameterization of the Condensation Process: A Theoretical Approach, Journal of Atmospheric Sciences, 48, 264–282, https://doi.org/10.1175/1520-0469(1991)048<0264:POTCPA>2.0.CO;2, 1991.
- Brenguier, J.-L., Pawlowska, H., Schüller, L., Preusker, R., Fischer, J., and Fouquart, Y.: Radiative Properties of Boundary Layer Clouds: Droplet Effective Radius versus Number Concentration, Journal of the Atmospheric Sciences, 57, 803–821, https://doi.org/10.1175/1520-0469(2000)057<0803:RPOBLC>2.0.CO;2, 2000.
- Capobianco, G. and Lee, M. D.: The Role of Weather in General Aviation Accidents: An Analysis of Causes, Contributing Factors and ISSUES, Proceedings of the Human Factors and Ergonomics Society Annual Meeting, 45, 190–194, https://doi.org/10.1177/154193120104500241, 2001.

- Cermak, J. and Bendix, J.: Detecting ground fog from space a microphysics-based approach, International Journal of Remote Sensing, 32, 3345–3371, https://doi.org/10.1080/01431161003747505, 2011.
- Chang, F.-L. and Li, Z.: Estimating the vertical variation of cloud droplet effective radius using multispectral near-infrared satellite measurements, Journal of Geophysical Research: Atmospheres, 107, AAC 7–1–AAC 7–12, https://doi.org/10.1029/2001JD000766, 2002.
- Costabloz, T., Burnet, F., Lac, C., Martinet, P., Delanoë, J., Jorquera, S., and Fathalli, M.: Vertical profiles of liquid water content in fog layers during the SOFOG3D experiment, Atmos. Chem. Phys., 25, 6539–6573, https://doi.org/10.5194/acp-25-6539-2025, 2025.
- Egli, S., Maier, F., Bendix, J., and Thies, B.: Vertical distribution of microphysical properties in radiation fogs
 A case study, Atmospheric Research, 151, 130–145, https://doi.org/10.1016/j.atmosres.2014.05.027, 2015.
- Fu, Q. and Liou, K. N.: On the Correlated k-Distribution Method for Radiative Transfer in Nonhomogeneous Atmospheres, Journal of Atmospheric 49, 2139-2156, https://doi.org/10.1175/1520ences. 0469(1992)049<2139:OTCDMF>2.0.CO;2, 1992.
- Fu, Q. and Liou, K. N.: Parameterization of the Radiative Properties of Cirrus Clouds, Journal of Atmospheric Sciences, 50, 2008–2025, https://doi.org/10.1175/1520-0469(1993)050<2008:POTRPO>2.0.CO;2, 1993.
- George, J. J.: Fog, American Meteorological Society, Boston, MA, 1179–1189, ISBN 978-1-940033-70-9, https://doi.org/10.1007/978-1-940033-70-9 95, 1951.
- Gilardoni, S., Massoli, P., Giulianelli, L., Rinaldi, M., Paglione, M., Pollini, F., Lanconelli, C., Poluzzi, V., Carbone, S., Hillamo, R., Russell, L. M., Facchini, M. C., and Fuzzi, S.: Fog scavenging of organic and inorganic aerosol in the Po Valley, Atmos. Chem. Phys., 14, 6967–6981, https://doi.org/10.5194/acp-14-6967-2014, 2014.
- Gultepe, I.: A Review on Weather Impact on Aviation Operations: Visibility, Wind, Precipitation, Icing, Journal of Airline Operations and Aviation Management, 2, https://doi.org/10.56801/jaoam.v2i1.1, 2023.
- Gultepe, I., Pearson, G., Milbrandt, J. A., Hansen, B., Platnick, S., Taylor, P., Gordon, M., Oakley, J. P., and Cober, S. G.: The Fog Remote Sensing and Modeling Field Project, Bulletin of the American Meteorological Society, 90, 341–360, https://doi.org/10.1175/2008BAMS2354.1, 2009.
- Hagan, D. H. and Kroll, J. H.: Assessing the accuracy of low-cost optical particle sensors using a physics-based approach, Atmos. Meas. Tech., 13, 6343–6355, https://doi.org/10.5194/amt-13-6343-2020, 2020.
- Han, S.-Q., Hao, T.-Y., Zhang, M., Yao, Q., Liu, J.-L., Cai, Z.-Y., and Li, X.-J.: Observation Analysis on Microphysics Characteristics of Long-lasting Severe Fog and Haze Episode at Urban Canopy Top, Aerosol and Air Quality Research, 18, 2475–2486, https://doi.org/10.4209/aaqr.2017.10.0416, 2018.
- Kasper, D. M.: Slots, Property Rights and Secondary Markets: Efficiency and Slot Allocation at US Airports, Taylor and Francis, https://doi.org/10.4324/9781315262963-27, 2016.
- Khain, A. P., Beheng, K. D., Heymsfield, A., Korolev, A., Krichak, S. O., Levin, Z., Pinsky, M., Phillips, V., Prabhakaran, T., Teller,

- A., van den Heever, S. C., and Yano, J.-I.: Representation of microphysical processes in cloud-resolving models: Spectral (bin) microphysics versus bulk parameterization, Reviews of Geophysics, 53, 247–322, https://doi.org/10.1002/2014RG000468, 2015.
- Lakra, K. and Avishek, K.: A review on factors influencing fog formation, classification, forecasting, detection and impacts, Rendiconti Lincei. Scienze Fisiche e Naturali, 33, 319–353, 2022.
- Maronga, B. and Bosveld, F. C.: Key parameters for the life cycle of nocturnal radiation fog: a comprehensive large-eddy simulation study, Quarterly Journal of the Royal Meteorological Society, 143, 2463–2480, https://doi.org/10.1002/qj.3100, 2017.
- Mason, J.: The Physics of Radiation Fog, Journal of the Meteorological Society of Japan Ser. II, 60, 486–499, https://doi.org/10.2151/jmsj1965.60.1_486, 1982.
- Mazoyer, M., Lac, C., Thouron, O., Bergot, T., Masson, V., and Musson-Genon, L.: Large eddy simulation of radiation fog: impact of dynamics on the fog life cycle, Atmospheric Chemistry and Physics, 17, 13017–13035, https://doi.org/10.5194/acp-17-13017-2017, 2017.
- Mazoyer, M., Burnet, F., and Denjean, C.: Experimental study on the evolution of droplet size distribution during the fog life cycle, Atmos. Chem. Phys., 22, 11305–11321, https://doi.org/10.5194/acp-22-11305-2022, 2022.
- Mohammadi, M., Nowak, J. L., Bertens, G., Moláček, J., Kumala, W., and Malinowski, S. P.: Cloud microphysical measurements at a mountain observatory: comparison between shadowgraph imaging and phase Doppler interferometry, Atmos. Meas. Tech., 15, 965–985, https://doi.org/10.5194/amt-15-965-2022, 2022.
- Nowak, J. L., Mohammadi, M., and Malinowski, S. P.: Applicability of the VisiSize D30 shadowgraph system for cloud microphysical measurements, Atmos. Meas. Tech., 14, 2615–2633, https://doi.org/10.5194/amt-14-2615-2021, 2021.
- Nurowska, K.: Microphysical and optical data of radiation fog in Strzyżów Valley, Poland, University of Warsaw [data set], https://doi.org/10.58132/WPKQNT, 2025.
- Nurowska, K., Mohammadi, M., Malinowski, S., and Markowicz, K.: Applicability of the low-cost OPC-N3 optical particle counter for microphysical measurements of fog, Atmos. Meas. Tech., 16, 2415–2430, https://doi.org/10.5194/amt-16-2415-2023, 2023.
- Okita, T.: Observations of the vertical structure of a stratus cloud and radiation fogs in relation to the mechanism of drizzle formation, Tellus, 14, 310–322, https://doi.org/10.3402/tellusa.v14i3.9556, 1962.
- Philip, A., Bergot, T., Bouteloup, Y., and Bouyssel, F.: The Impact of Vertical Resolution on Fog Forecasting in the Kilometric-Scale Model AROME: A Case Study and Statistics, Weather and Forecasting, 31, 1655–1671, https://doi.org/10.1175/WAF-D-16-0074.1, 2016.
- Pinnick, R. G., Hoihjelle, D. L., Fernandez, G., Stenmark, E. B., Lindberg, J. D., Hoidale, G. B., and Jennings, S. G.: Vertical Structure in Atmospheric Fog and Haze and Its Effects on Visible and Infrared Extinction, Journal of Atmospheric Sciences, 35, 2020–2032, https://doi.org/10.1175/1520-0469(1978)035<2020:VSIAFA>2.0.CO;2, 1978.

- Pithani, P., Ghude, S., Naidu, c., Kulkarni, R., Steeneveld, G.-J., Sharma, A., Prabha, T., Chate, D., Gultepe, I., Jenamani, R., and Rajeevan, M.: WRF model Prediction of a dense fog event occurred during Winter Fog Experiment (WIFEX), Pure and Applied Geophysics, 176, 1827–1846, https://doi.org/10.1007/s00024-018-2053-0, 2019.
- Poku, C., Ross, A. N., Hill, A. A., Blyth, A. M., and Shipway, B.: Is a more physical representation of aerosol activation needed for simulations of fog?, Atmos. Chem. Phys., 21, 7271–7292, https://doi.org/10.5194/acp-21-7271-2021, 2021.
- Price, J.: Radiation Fog. Part I: Observations of Stability and Drop Size Distributions, Boundary-Layer Meteorology, 139, 167–191, https://doi.org/10.1007/s10546-010-9580-2, 2011.
- Román-Cascón, C., Yagüe, C., Sastre, M., Maqueda, G., Salamanca, F., and Viana, S.: Observations and WRF simulations of fog events at the Spanish Northern Plateau, Adv. Sci. Res., 8, 11–18, https://doi.org/10.5194/asr-8-11-2012, 2012.
- Stevens, S. E.: Trends in Instrument Flight Rules (IFR) Conditions at Major Airports in the United States, Journal of Applied Meteorology and Climatology, 58, 615–620, https://doi.org/10.1175/JAMC-D-18-0301.1, 2019.
- Thoma, C., Schneider, W., Masbou, M., and Bott, A.: Integration of Local Observations into the One Dimensional Fog Model PAFOG, Pure and Applied Geophysics, 169, 881–893, https://doi.org/10.1007/s00024-011-0357-4, 2011.
- Toledo, F., Haeffelin, M., Wærsted, E., and Dupont, J.-C.: A new conceptual model for adiabatic fog, Atmos. Chem. Phys., 21, 13099–13117, https://doi.org/10.5194/acp-21-13099-2021, 2021.
- Wærsted, E. G., Haeffelin, M., Dupont, J.-C., Delanoë, J., and Dubuisson, P.: Radiation in fog: quantification of the impact on fog liquid water based on ground-based remote sensing, Atmos. Chem. Phys., 17, 10811–10835, https://doi.org/10.5194/acp-17-10811-2017, 2017.
- Wendish, M., Mertes, S., Heintzenberg, J., Wiedensohler, A., Schell, D., Wobrock, W., Frank, G., Martinsson, B. G., Fuzzi, S., Orsi, G., Kos, G., and Berner, A.: Drop size distribution and LWC in Po valley fog, Contributions to Atmospheric Physics, 71, 87–100, https://www.scopus.com/inward/record.uri?eid=2-s2.0-0031779779&partnerID=40&md5=9b5423094749ae926835f315751c4503 (last access: 20 December 2024), 1998.
- Yau, M. and Rogers, R.: A Short Course in Cloud Physics, Elsevier Science, ISBN 9780080570945, https://books.google.pl/books?id=ClKbCgAAQBAJ (last access: 20 December 2024), 1996.
- Ye, X., Wu, B., and Zhang, H.: The turbulent structure and transport in fog layers observed over the Tianjin area, Atmospheric Research, 153, 217–234, https://doi.org/10.1016/j.atmosres.2014.08.003, 2015.
- Zhou, B., Du, J., Gultepe, I., and Dimego, G.: Forecast of Low Visibility and Fog from NCEP: Current Status and Efforts, Pure and Applied Geophysics, 169, 895–909, https://doi.org/10.1007/s00024-011-0327-x, 2012.